



## Post-buckling of fiber-reinforced soft tissues

Yang Liu<sup>a,b,c</sup>, Rui-Cheng Liu<sup>a</sup>, Wanyu Ma<sup>a</sup>, Alain Goriely<sup>b</sup>

<sup>a</sup> Department of Mechanics, School of Mechanical Engineering, Tianjin University, Tianjin 300350, China

<sup>b</sup> Mathematical Institute, University of Oxford, Oxford, OX2 6GG, UK

<sup>c</sup> National Key Laboratory of Vehicle Power System, Tianjin 300350, China

### ARTICLE INFO

#### Keywords:

Surface wrinkling  
Fiber-reinforcement materials  
Film/substrate bilayers  
Bifurcation  
Weakly nonlinear analysis  
Nonlinear elasticity

### ABSTRACT

Fiber-reinforcement is a universal feature of many biological tissues. It involves the interplay between fiber stiffness, fiber orientation, and the elastic properties of the matrix, influencing pattern formation and evolution in layered tissues. Here, we investigate the deformation of a compressed film bonded to a half-space, where either the film or the substrate exhibits anisotropy. Within the framework of finite elasticity, we formulate nonlinear incremental equations, enabling linear and weakly nonlinear analyses. These analyses yield exact bifurcation conditions and an amplitude equation for surface wrinkling. In particular, for a simple fiber-reinforced model, we show that the bifurcation can be supercritical or subcritical depending on the ratio between the substrate and the film moduli. These findings underscore the pivotal role of fiber-reinforcement in shaping pattern formation in anisotropic tissues and provide insights into the morphological evolution of biological tissues.

### 1. Introduction

Bilayered structures, where a thin but stiff film adheres to a thick and compliant substrate, are widely observed in nature and engineering applications (Genzer and Groenewold, 2006; Li et al., 2012; Goriely, 2017). This type of structure is often susceptible to wrinkling formation, which can be induced through compressive stresses, generated from either compression (Chen and Hutchinson, 2004; Kim et al., 2011), thermal expansion (Barnes et al., 2023), growth (Li et al., 2011), or swelling (Liu et al., 2022a). For instance, it is well appreciated that human skins initiate wrinkles with aging (Zhao et al., 2020; Chavoshnejad et al., 2021; Lynch et al., 2022), brain develops complex folds due to the fast expansion of the cortical layer (Budday et al., 2015; Holland et al., 2020; Wang et al., 2021), and fruits and vegetables form wrinkles because of differential growth between pericarp and sarcocarp (Yin et al., 2009; Dai and Liu, 2014).

Both theoretically and experimentally, a film/substrate bilayer serves as a foundational model for investigating complex pattern formation in layered structures. Consequently, significant effort has been devoted to determining the critical conditions for surface wrinkling by solving the eigenvalue problem associated with the linearized governing equations (Shield et al., 1994; Bigoni et al., 1997; Cai and Fu, 2000; Liu and Dai, 2014; Zhang, 2017; Alawiye et al., 2019; Liu et al., 2024b). This approach allows the simultaneous determination of critical loads and the corresponding wrinkled patterns. However, post-bifurcation behavior can only be analyzed within the nonlinear regime. In the context of finite elasticity, this analysis is commonly conducted by superimposing an incremental deformation onto a finitely deformed state, a method now referred to as incremental theory (Biot, 1965; Ogden, 1984; Goriely, 2017). Following this original analysis, Cai and Fu (1999) derived an amplitude equation for surface wrinkling

\* Corresponding author at: Mathematical Institute, University of Oxford, Oxford, OX2 6GG, UK.

E-mail addresses: [liuy3@maths.ox.ac.uk](mailto:liuy3@maths.ox.ac.uk), [tracy\\_liu@tju.edu.cn](mailto:tracy_liu@tju.edu.cn) (Y. Liu).

<sup>1</sup> All authors contributed equally to this work.

<https://doi.org/10.1016/j.jmps.2025.106220>

Received 3 February 2025; Received in revised form 26 April 2025; Accepted 31 May 2025

Available online 17 June 2025

0022-5096/© 2025 The Authors. Published by Elsevier Ltd. This is an open access article under the CC BY license (<http://creativecommons.org/licenses/by/4.0/>).

of a neo-Hookean film bonded to another neo-Hookean half-space and identified a critical modulus ratio of two layers where a transition between supercritical and subcritical bifurcations takes place. Later, they investigated the effect of compressibility and secondary period-doubling bifurcations (Cai and Fu, 2019; Fu and Cai, 2015). Hutchinson (2013) re-discovered the same transition shown in Cai and Fu (1999) by including pre-stretch effects. For three-dimensional wrinkling, Ciarletta (2014) performed a weakly nonlinear analysis for soft layers with equi-biaxial strain and analytically studied the wrinkle to fold transition. Using the finite growth theory (Ben Amar and Goriely, 2005), Ciarletta and Fu (2015) developed a semi-analytical method for a growing layer, and later Jin et al. (2019) extended the nonlinear analysis to tubular tissues to trace the post-buckling evolution. Recently, Alawiye et al. (2020) performed the post-buckling analysis assuming that the compressive stress can be generated by either compression or the growth of thin film.

The aforementioned studies reveal that when the film and substrate possess similar elastic moduli, the bifurcation transitions to a subcritical nature. Analyzing the post-buckling behavior in cases of subcritical bifurcation presents significant theoretical challenges, as multiple modes often interact near the critical point, complicating the analysis. Fu and Ciarletta (2015) employed a Fourier expansion to derive nonlinear amplitude equations for subcritical bifurcation, revealing that a localized solution can emerge as the limit of modulated periodic solutions. More recently, Shen et al. (2024) examined a similar problem by considering growth effects and numerically identified distinct characteristic domains where different patterns exist.

Wrinkles in layered structures continue to attract significant research interest across diverse fields due to their widespread applications in flexible electronics, sensors, and related technologies (Sun et al., 2006; Cui, 2016; Lee et al., 2022), surface engineering (Yang et al., 2010; Zhang et al., 2012; Li et al., 2017; Lee et al., 2021), elastic metamaterials (Liu et al., 2022b; Han et al., 2024), and bio-inspired design (Tan et al., 2020; Zhao and Fang, 2024). As a result, many different features of the problem have been studied, including the influence of viscosity (Huang, 2005; Liu et al., 2022c), multi-layering (Cheng et al., 2014; Zhou et al., 2022), growth or swelling (Budday et al., 2014; Zhao et al., 2015; Eskandari et al., 2016; Polukhov et al., 2023), grading modulus (Chen et al., 2017; Liu et al., 2020), curvature (Jia et al., 2018; Liu et al., 2025) and pattern selection in three dimensions (Cheewaruangroj and Biggins, 2019).

This paper focuses on anisotropic bilayers. In engineering applications, anisotropy can be used to tune pattern selection (Im and Huang, 2008; Song, 2010; Yin et al., 2018). Similarly, many biological tissues, such as skin and arteries, are naturally endowed with fibers, making them intrinsically anisotropic (Chavoshnejad et al., 2021; Hill et al., 2012). Consequently, it is of fundamental importance to develop mechanical models that address buckling instabilities and post-buckling evolution, providing insights into the formation and progression of various morphological patterns.

Im and Huang (2008) studied the wrinkled pattern of anisotropic films resting on viscoelastic substrates. Based on the Föppl-von Kármán plate theory, Yin et al. (2018) explored analytically and numerically pattern formation and evolution in an orthotropic film bonded to a compliant substrate. Using linear elasticity, Guo and Nie (2023) investigated the influence of fiber orientation on surface wrinkling in anisotropic substrates. However, it has been noted that the surface instability of many biological tissues is often associated with highly nonlinear constitutive responses (Pocivavsek et al., 2018), highlighting the necessity of addressing these phenomena within the framework of finite elasticity.

To account for fiber-reinforcement, one of the most widely used models is the Holzapfel–Gasser–Ogden (HGO) model, which was developed for arteries (Holzapfel et al., 2000; Gasser et al., 2006; Holzapfel and Ogden, 2010). The HGO model is also applicable to various biological tissues exhibiting collagen fiber distributions (Holzapfel et al., 2019). Notably, a key assumption of the HGO model is that fibers are nearly inextensible and incapable of bearing compression. To address limitations associated with fiber extensibility, Horgan and Saccomandi (2005), inspired by the Gent model for natural rubber (Gent, 1996), proposed a constitutive theory for fiber-reinforced incompressible solids, accommodating fibers with finite extensibility. Building on these advancements, Stewart et al. (2016) explored brain morphogenesis by analyzing pattern evolution in a film bonded to a fiber-reinforced substrate under compression. They found that the folding pattern is nearly independent of the fiber orientation. Nguyen et al. (2020) conducted a detailed analysis of the effects of fiber orientation, fiber stiffness, and dispersion on the onset of surface wrinkling in a neo-Hookean film bonded to an HGO substrate. Additionally, they employed finite element simulations to investigate the post-buckling evolution. More recently, Mirandola et al. (2023) derived a scaling law to characterize the critical wrinkled state in anisotropic bilayers where the substrate is reinforced by two families of fibers. Altun et al. (2023) numerically explored growth-induced surface wrinkling when the film has a single family of fibers, using a three-dimensional framework based on a five-field Hu–Washizu-type mixed variational formulation.

We emphasize that all the aforementioned studies on the post-buckling behavior of anisotropic film/substrate bilayers have primarily relied on finite element simulations. Analytical solutions for post-buckling behavior remain scarce, and the bifurcation characteristics of the initial instability, particularly the role of anisotropy, are not yet fully understood. This paper aims to address these gaps by performing an analytical post-buckling analysis. Additionally, we seek to develop a unified framework capable of analyzing cases where either the thin film or the substrate is anisotropic. This approach will enable a systematic and qualitative comparison between the two scenarios, providing insights into the influence of anisotropy on instability and pattern formation.

The remainder of this paper is organized as follows. Section 2 presents a summary of the fundamental equations. In Section 3, we conduct a linear bifurcation analysis to determine the exact bifurcation condition. The effects of fiber orientation and stiffness on the critical state are examined, and mode transitions are discussed. Section 4 focuses on a weakly nonlinear analysis, where an analytical amplitude equation is derived. The transition between supercritical and subcritical bifurcations is identified, and the post-buckling evolution is analyzed in detail. We provide several comparisons with existing studies and outline potential directions for future work in Section 5. Finally, conclusions are provided in Section 6.

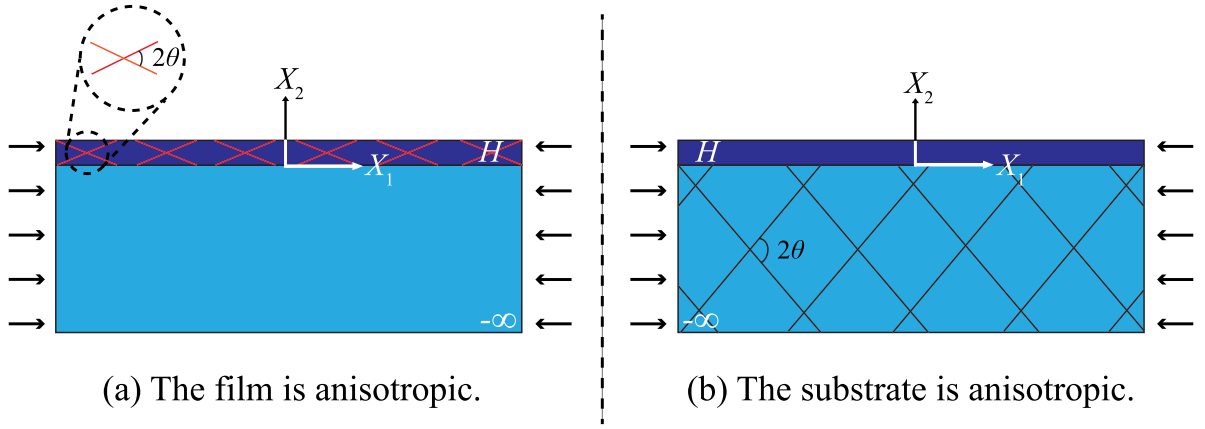


Fig. 1. Geometry of a bilayer in the reference configuration  $B_0$  where either the film or the substrate is composed of a fiber-reinforced anisotropic material.

## 2. Problem formulation and incremental theory

Consider an elastic bilayer where either the film or the substrate is an anisotropic material and both incompressible layers are subject to the same axial compression as shown in Fig. 1. Initially, the film has a thickness  $H$ , and the substrate is a half-space. Anisotropy is introduced by two families of fibers oriented at an angle  $\pm\theta$  with respect to  $X_1$ , the horizontal axis. We use the Cartesian coordinate system and adopt a plane-strain condition in the  $(X_1, X_2)$ -plane.

The bilayer is subject to a compressive stress along the  $X_1$ -direction, leading for small values of the compression to a homogeneous deformation occurs in which the thickness of the film increases to  $h$ . For larger values, we expect that an instability will take place and the homogeneous deformation will be replaced by a surface wrinkling profile at a critical compressive strain. Here, we focus on the post-buckling behavior by performing a weakly nonlinear analysis using incremental theory (Ogden, 1984; Fu and Ogden, 1999). We begin by formulating the nonlinear incremental equations for a general hyperelastic material.

We use  $\mathbf{X} = (X_1, X_2)$  and  $\mathbf{x} = (x_1, x_2)$  to represent the position vectors of a material point in the stress-free reference configuration  $B_0$  and in the homogeneously stressed configuration  $B_r$ , respectively. Subsequently, we superimpose a small-amplitude deformation on  $B_r$ , leading to the final configuration denoted by  $B_t$ , with associated position vector  $\tilde{\mathbf{x}} = (\tilde{x}_1, \tilde{x}_2)$  that can be written as

$$\tilde{\mathbf{x}} = \mathbf{x} + \mathbf{u}(\mathbf{x}), \tag{2.1}$$

where  $\mathbf{u}$  is the incremental displacement from  $B_r$  to  $B_t$ . Introducing the common orthonormal basis in all three configurations  $\{\mathbf{e}_1, \mathbf{e}_2\}$ , we have  $\mathbf{u} = u_1 \mathbf{e}_1 + u_2 \mathbf{e}_2$ .

The deformation gradients  $\mathbf{F}$  from  $B_0 \rightarrow B_t$  and  $\bar{\mathbf{F}}$  from  $B_0 \rightarrow B_r$ , are given by

$$F_{iA} = \frac{\partial \tilde{x}_i}{\partial X_A}, \quad \bar{F}_{iA} = \frac{\partial x_i}{\partial X_A}. \tag{2.2}$$

They are related by

$$F_{iA} = (\delta_{ij} + u_{i,j}) \bar{F}_{jA}, \tag{2.3}$$

where  $\delta_{ij}$  is the usual Kronecker delta and we define a lower case  $j$  behind a comma to be the derivative with respect to  $x_j$  while a capital  $A$  letter would indicate the derivative with respect to  $X_A$ .

The incompressibility constraint yields

$$\det \mathbf{F} = 1, \quad \det \bar{\mathbf{F}} = 1. \tag{2.4}$$

The left and right Cauchy–Green deformation tensors read

$$\mathbf{B} = \mathbf{F}\mathbf{F}^T, \quad \mathbf{C} = \bar{\mathbf{F}}^T\bar{\mathbf{F}}, \tag{2.5}$$

with similar expressions in  $B_r$ .

The first Piola–Kirchhoff stress tensors in  $B_r$  and  $B_t$  are given by

$$\pi_{iA} = \frac{\partial W(\mathbf{F})}{\partial F_{iA}} - p F_{Ai}^{-1}, \quad \bar{\pi}_{iA} = \frac{\partial W(\bar{\mathbf{F}})}{\partial \bar{F}_{iA}} - \bar{p} \bar{F}_{Ai}^{-1}, \tag{2.6}$$

where  $W$  denotes the strain–energy density,  $p$  and  $\bar{p}$  are the Lagrange multipliers enforcing the incompressibility conditions in (2.4).

In the absence of body forces, the equilibrium conditions for both states  $B_r$  and  $B_t$  are

$$\bar{\pi}_{iA,A} = 0, \quad \pi_{iA,A} = 0, \tag{2.7}$$

where we adopt the summation convention over repeated indices unless specified otherwise.

To address the stability of  $B_r$ , we introduce the incremental stress tensor

$$\chi = (\boldsymbol{\pi} - \bar{\boldsymbol{\pi}}) \bar{\mathbf{F}}^\top, \quad \text{or} \quad \chi_{ij} = (\pi_{iA} - \bar{\pi}_{iA}) \bar{F}_{jA}. \tag{2.8}$$

In view of (2.7), (2.8) and by virtue of the identity  $\text{div } \bar{\mathbf{F}} = \mathbf{0}$ , we arrive at the incremental equilibrium equation

$$\text{div } \chi^\top = \mathbf{0}, \quad \text{or} \quad \chi_{ij,j} = 0. \tag{2.9}$$

where ‘div’ is the divergence operator in  $B_r$ .

For an infinitesimal incremental displacement  $\mathbf{u}(\mathbf{x})$ , we expand  $\chi$  in the incremental displacement to obtain

$$\begin{aligned} \chi_{ij} = & \mathcal{A}_{jilk}^1 u_{k,l} + \frac{1}{2} \mathcal{A}_{jilknm}^2 u_{k,l} u_{m,n} + \frac{1}{6} \mathcal{A}_{jilknmqp}^3 u_{k,l} u_{m,n} u_{p,q} \\ & + \bar{p} (u_{j,i} - u_{j,k} u_{k,i} + u_{j,k} u_{k,l} u_{l,i}) - p^* (\delta_{ji} - u_{j,i} + u_{j,k} u_{k,i}) + \mathcal{O}(|u_{i,j}|^4), \end{aligned} \tag{2.10}$$

where  $\mathcal{A}^1, \mathcal{A}^2, \mathcal{A}^3$  are, respectively, the first-, second-, third-order instantaneous elastic moduli and  $p^* = p - \bar{p}$  is the pressure increment. In the above expression, we retain nonlinearities up to the third order, as required in a generic weakly nonlinear analysis (Cai and Fu, 1999; Fu and Ogden, 1999; Jin et al., 2019; Alawiye et al., 2020).

Explicitly, the incremental elastic moduli are (Chadwick and Ogden, 1971; Ogden, 1984; Fu and Ogden, 1999).

$$\begin{aligned} \mathcal{A}_{jilk}^1 &= \bar{F}_{jA} \bar{F}_{lB} \left. \frac{\partial^2 W}{\partial F_{iA} \partial F_{kB}} \right|_{\mathbf{F}=\bar{\mathbf{F}}}, \\ \mathcal{A}_{jilknm}^2 &= \bar{F}_{jA} \bar{F}_{lB} \bar{F}_{nC} \left. \frac{\partial^3 W}{\partial F_{iA} \partial F_{kB} \partial F_{mC}} \right|_{\mathbf{F}=\bar{\mathbf{F}}}, \\ \mathcal{A}_{jilknmqp}^3 &= \bar{F}_{jA} \bar{F}_{lB} \bar{F}_{nC} \bar{F}_{qD} \left. \frac{\partial^4 W}{\partial F_{iA} \partial F_{kB} \partial F_{mC} \partial F_{pD}} \right|_{\mathbf{F}=\bar{\mathbf{F}}}. \end{aligned} \tag{2.11}$$

On substituting (2.10) into (2.9), we obtain the incremental equations up to third order:

$$\mathcal{A}_{jilk}^1 u_{k,l,j} + \mathcal{A}_{jilknm}^2 u_{m,n} u_{k,l,j} + \frac{1}{2} \mathcal{A}_{jilknmqp}^3 u_{m,n} u_{p,q} u_{k,l,j} - p_{,j}^* (\delta_{ji} - u_{j,i} + u_{j,m} u_{m,i}) + \mathcal{O}(|u_{i,j}|^4) = 0. \tag{2.12}$$

In addition, the incompressibility condition (2.4)<sub>1</sub> gives (Fu and Ogden, 1999)

$$u_{i,i} = \frac{1}{2} u_{m,n} u_{n,m} - \frac{1}{2} (u_{i,i})^2 - \det(u_{m,n}). \tag{2.13}$$

Currently, we have formulated the general governing equations in (2.12) and (2.13) for further analysis. Note that we still need to give the incremental boundary conditions.

We from now on focus on the surface wrinkling in compressive bilayers where either the layer or the substrate may be anisotropic, as shown in Fig. 1. To distinguish between two layers, we denote quantities associated with the half-space by using an over-hat, whereas quantities without a hat belong to the film. For quantities that take the same form in both layers, the hat is omitted if the quantity is evaluated in the domain of the half-space. For example, the deformation gradient of the homogeneous deformation is valid for both layers and we simply write

$$\bar{\mathbf{F}} = \text{diag} \{ \lambda, \lambda^{-1} \}, \tag{2.14}$$

where  $\lambda$  is the principal stretch in the  $X_1$ -direction and  $1/\lambda$  is the principal stretch in the  $X_2$ -direction to satisfy the incompressibility constraint. Therefore, the deformed thickness of the film becomes

$$h = \frac{H}{\lambda}. \tag{2.15}$$

For boundary conditions, we consider a traction-free top surface, perfect bonding at the interface, and zero displacement at infinity. In doing so, the incremental boundary conditions and continuity conditions are summarized as follows

$$\left. \begin{aligned} \chi_{i2} &= 0, & \text{on } x_2 = h, \\ \hat{u}_i &= u_i, & \hat{\chi}_{i2} = \chi_{i2}, & \text{on } x_2 = 0, \\ \hat{u}_i &\rightarrow 0, & \text{as } x_2 \rightarrow -\infty, \end{aligned} \right\} \quad i = 1, 2. \tag{2.16}$$

Eqs. (2.12), (2.13) and their counterparts for the half-space, together with (2.16), formulate the incremental system governing wrinkling initiation and evolution in compressive bilayers. Later, we first perform a linear analysis and then a weakly nonlinear analysis.

### 3. Linear bifurcation analysis

We perform a linear bifurcation analysis to find the critical compressive strain. To this end, we use the linear part of the incremental system established in the previous section. To avoid redundant derivations, we briefly summarize the general result of the eigenvalue problem stemming from the linearized versions of (2.12) and (2.13), which are given by

$$\mathcal{A}_{jilk}^1 u_{k,l,j} - p_{,i}^* = 0, \quad u_{i,i} = 0, \quad -\infty < x_2 \leq h. \tag{3.1}$$

It is convenient to introduce a *stream* function  $\psi(x_1, x_2)$  such that

$$u_1 = \psi_{,2}, \quad u_2 = -\psi_{,1}. \tag{3.2}$$

By substituting (3.2) into (3.1) and then eliminating  $p^*$  through cross-differentiation, we obtain the fourth-order equation

$$\mathcal{A}_{2121}^1 \psi_{,2222} - (\mathcal{A}_{1111}^1 + \mathcal{A}_{2222}^1 - 2\mathcal{A}_{1122}^1 - 2\mathcal{A}_{1221}^1) \psi_{,1122} + \mathcal{A}_{1212}^1 \psi_{,1111} = 0. \tag{3.3}$$

We look for a traveling wave solution to (3.3) in the form

$$\psi = \zeta (nx_2) e^{inx_1}, \tag{3.4}$$

where  $n$  is the wavenumber and ‘ $i$ ’ is the imaginary unit. Inserting (3.4) into (3.3) yields a fourth-order ordinary differential equation of  $\zeta(nx_2)$  with the characteristic equation given by

$$\mathcal{A}_{2121}^1 s^4 - (\mathcal{A}_{1111}^1 + \mathcal{A}_{2222}^1 - 2\mathcal{A}_{1122}^1 - 2\mathcal{A}_{1221}^1) s^2 + \mathcal{A}_{1212}^1 = 0, \tag{3.5}$$

where  $s$  is the eigenvalue and the general solutions for  $\zeta(nx_2)$  and  $\hat{\zeta}(nx_2)$  are

$$\begin{aligned} \zeta(nx_2) &= \sum_{j=1}^4 Q_j \exp (ns_j x_2), & x_2 \in (0, h), \\ \hat{\zeta}(nx_2) &= Q_5 \exp (n\hat{s}_1 x_2) + Q_6 \exp (n\hat{s}_2 x_2), & x_2 \in (-\infty, 0), \end{aligned} \tag{3.6}$$

where  $Q_1$  to  $Q_6$  are constants, and without loss of generality we have removed solutions that do not decay at infinity for the half-space. Hence,  $s_i$  and  $\hat{s}_i$  ( $i = 1, 2$ ) have positive real parts.

From (2.16), we write down the linearized incremental boundary conditions and continuity conditions:

$$\left. \begin{aligned} T_i^{(l)} &= 0, & \text{on } x_2 = h, \\ \hat{u}_i &= u_i, \quad \hat{T}_i^{(l)} = T_i^{(l)}, & \text{on } x_2 = 0, \end{aligned} \right\} \quad i = 1, 2, \tag{3.7}$$

where

$$T_i^{(l)} = \mathcal{A}_{2ilk}^1 u_{k,l} + \bar{p} u_{2,i} - p^* \delta_{2i}, \quad \hat{T}_i^{(l)} = \hat{\mathcal{A}}_{2ilk}^1 \hat{u}_{k,l} + \hat{p} \hat{u}_{2,i} - \hat{p}^* \delta_{2i}. \tag{3.8}$$

A direct substitution of (3.6) into (3.7) gives rise to the linear system:

$$\mathbf{G}\mathbf{Q} = 0, \tag{3.9}$$

where  $\mathbf{G}$  is a  $6 \times 6$  matrix whose elements are dependent on the principal stretch  $\lambda$  and the material parameters once  $W$  and  $\hat{W}$  are specified, and  $\mathbf{Q} = [Q_1, Q_2, Q_3, Q_4, Q_5, Q_6]^T$ . The existence of a non-trivial solution requires

$$\det \mathbf{G} = 0, \tag{3.10}$$

which characterizes the values of the bifurcation parameter at which an instability takes place.

We emphasize that the thin film or the half-space is anisotropic. For the isotropic material, we adopt a neo-Hookean law with strain energy function given by

$$W_{\text{nH}} = \frac{\mu_{\text{nH}}}{2} (\text{tr } \mathbf{B} - 3), \tag{3.11}$$

where  $\mu_{\text{nH}}$  is the shear modulus and  $\mathbf{B}$  can be found in (2.5)<sub>1</sub>. In the subsequent analysis, a subscript ‘nH’ will indicate that the neo-Hookean model (3.11) is used.

Anisotropy arises from two families of fibers, as illustrated in Fig. 1 for which we adopt the HGO model (Holzapfel et al., 2000):

$$W_{\text{HGO}} = \frac{\mu_{\text{HGO}}}{2} (I_1 - 3) + \frac{k_1}{2k_2} \left( \exp[(I_4 - 1)^2 k_2] + \exp[(I_6 - 1)^2 k_2] - 2 \right), \tag{3.12}$$

where  $\mu_{\text{HGO}}$  is also the ground-state shear modulus,  $k_1$  corresponds to fiber stiffness (with stress unit), and  $k_2$  is a dimensionless parameter that controls the nonlinear response of the fiber. The principal invariants  $I_i$  ( $i = 1, 4, 6$ ) are defined as

$$I_1 = \text{tr } \mathbf{C}, \quad I_4 = \mathbf{M} \cdot \mathbf{C}\mathbf{M}, \quad I_6 = \mathbf{M}' \cdot \mathbf{C}\mathbf{M}', \tag{3.13}$$

where  $\mathbf{M}$  and  $\mathbf{M}'$  are the directions of the two fibers families, and  $\mathbf{C}$  is the right Cauchy–Green deformation tensor (2.5)<sub>2</sub>. Similarly, the subscript ‘HGO’ is correlated to (3.12). It can be seen that for  $k_1 = 0$  the HGO model is identical to the neo-Hookean model.

We assume that the fibers are symmetric with respect to the  $X_1$ -axis and oriented at an angle  $\theta$ , such that

$$\mathbf{M} = \cos \theta \mathbf{e}_1 + \sin \theta \mathbf{e}_2, \quad \mathbf{M}' = \cos \theta \mathbf{e}_1 - \sin \theta \mathbf{e}_2. \tag{3.14}$$

By use of (2.14), the two principal invariants  $I_4$  and  $I_6$  in homogeneous deformation are expressed as

$$I_4 = I_6 = \lambda^2 \cos^2 \theta + \frac{\sin^2 \theta}{\lambda^2}. \tag{3.15}$$

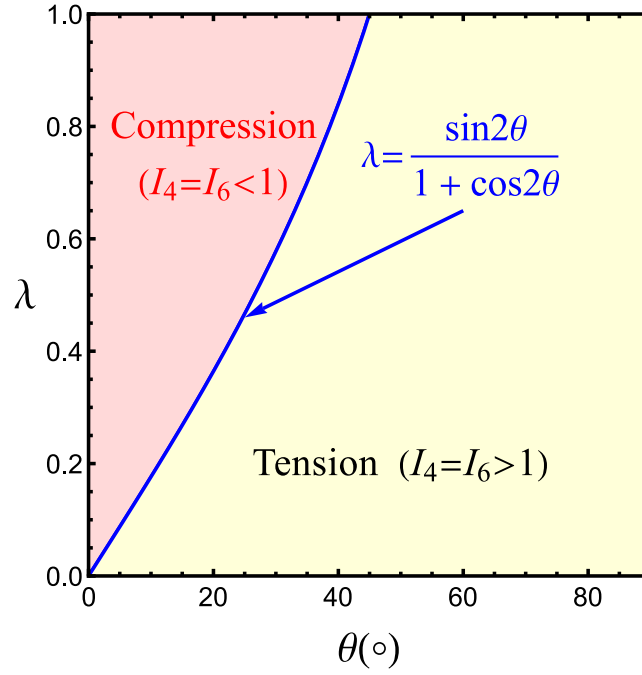


Fig. 2. Transition between fiber compression and fiber tension during the uniform deformation.

As discussed in Holzapfel et al. (2000), the fiber reinforcement becomes inactive when either  $I_4 \leq 1$  or  $I_6 \leq 1$ , namely, fibers cannot support compressive stresses, in which case the associated response reduces to the isotropic case. In view of this, we solve the equation  $I_4 - 1 = 0$  to obtain the transition compression ratio given by

$$\lambda = \frac{\sin 2\theta}{1 + \cos 2\theta}. \tag{3.16}$$

We further plot in Fig. 2 the compression and tension regions for the fibers. The material is reinforced only for fiber angles and compression within the light yellow region. This is the region where we perform our analysis. Otherwise, the neo-Hookean model will be employed and the problem reduces to the standard isotropic wrinkling problem (Alawiye et al., 2020). Specifically, when  $\lambda = 1$  the corresponding fiber angle is  $\theta = 45^\circ$  as derived from (3.16).

During a homogeneous deformation, we impose the zero traction condition at  $x_2 = h$  and ensure traction continuity at the interface  $x_2 = 0$ . This condition specifies the Lagrange multipliers  $\bar{p}_{nH}$  and  $\bar{p}_{HGO}$  from  $\bar{\pi}_{22} = 0$  as follows

$$\begin{aligned} \bar{p}_{nH} &= \frac{\mu_{nH}}{\lambda^2}, \\ \bar{p}_{HGO} &= \frac{\mu_{HGO}}{\lambda^2} + \frac{4k_1 \sin^2 \theta}{\lambda^2} \left( \lambda^2 \cos^2 \theta - 1 + \frac{\sin^2 \theta}{\lambda^2} \right) \left( \exp \left[ k_2 \left( \lambda^2 \cos^2 \theta - 1 + \frac{\sin^2 \theta}{\lambda^2} \right)^2 \right] \right). \end{aligned} \tag{3.17}$$

The latter is consistent with the result in Mirandola et al. (2023). Furthermore, these two expressions are universally valid regardless of the location of neo-Hookean material and the HGO material.

We consider two scenarios:

- Case I: a neo-Hookean half-space coated by an HGO film,
- Case II: an HGO half-space coated by a neo-Hookean film.

To avoid confusion, we emphasize the consistency of notations by making the following connections:

$$\begin{cases} \text{case I : } \hat{W} = W_{nH}, \hat{p} = \bar{p}_{nH}, \hat{\mu} = \mu_{nH}, W = W_{HGO}, \bar{p} = \bar{p}_{HGO}, \mu = \mu_{HGO}, \text{ and so on,} \\ \text{case II : } \hat{W} = W_{HGO}, \hat{p} = \bar{p}_{HGO}, \hat{\mu} = \mu_{HGO}, W = W_{nH}, \bar{p} = \bar{p}_{nH}, \mu = \mu_{nH}, \text{ and so on.} \end{cases} \tag{3.18}$$

Further, we introduce the ratio of the shear modulus of the half-space to that of the thin film  $r = \hat{\mu}/\mu$ . We further measure all stress quantities with respect to  $\mu$ , which amounts to take  $\mu = 1$  and stresses dimensionless without loss of generality. Hence in the subsequent analysis  $k_1$  will be dimensionless when it is specified by a value.

When the neo-Hookean material model (3.11) is used, the eigenvalues of (3.5) are given by  $s_1 = 1, s_2 = \lambda^2, s_3 = -1, s_4 = -\lambda^2$ . However, for the HGO model (3.12), the eigenvalues have cumbersome expressions that will not be explicitly presented. Additionally,

we may encounter repeated roots that lead to the coefficient matrix  $\mathbf{G}$  being multiplied by a zero factor, which will result in extraneous solutions that need proper care.

The bifurcation condition (3.10) can be recast as

$$\det \mathbf{G} = \Xi(\lambda, nh, r, k_1, k_2, \theta) = 0, \tag{3.19}$$

where  $nh$  can be regarded as a unified parameter as they never appear individually (Cai and Fu, 1999; Alawiye et al., 2019; Liu et al., 2024a). Now the bifurcation condition (3.19) is related to the principal stretch  $\lambda$ , the wavenumber  $nh$ , the modulus ratio  $r$ , and the anisotropy parameters  $(k_1, k_2, \theta)$ .

Once the parameters  $r, k_1, k_2$  and  $\theta$  are given, it is convenient to plot the bifurcation curve of  $\lambda$  versus the wavenumber  $nh$ . If  $r \ll 1$ , namely, the film is extremely stiffer than the substrate, it is known that the  $\lambda$ - $nh$  curve will attain a maximum which identifies the critical stretch  $\lambda_{cr}$  and the critical wavenumber  $(nh)_{cr}$  (Cai and Fu, 1999; Liu and Dai, 2014; Alawiye et al., 2019). Furthermore, the critical state can be determined from (3.19) and

$$\frac{\partial \Xi}{\partial (nh)} = 0. \tag{3.20}$$

As  $r$  approaches to 1, i.e., the film and the substrate share a similar modulus and a transition between supercritical and subcritical bifurcations may occur, but this can only be tackled in the nonlinear regime (Cai and Fu, 1999; Hutchinson, 2013; Jin et al., 2019; Alawiye et al., 2020), which will be investigated in the next section.

In the following, we will explore separately the critical state for two scenarios by focusing on the allowable parametric domain  $r \ll 1$  where surface wrinkling would be more favorable.

### 3.1. Case I: HGO film/neo-Hookean substrate

We consider the first scenario in which the film is fiber-reinforced. Then, the bifurcation condition (3.19) and Eq. (3.20) will yield the values of the critical stretch  $\lambda_{cr}$  and the critical wavenumber  $(nh)_{cr}$  for given material parameters. We find that the parameter  $k_2$  has a marginal influence on the critical state so in this subsection it will be given the literature value of  $k_2 = 0.8393$  (Holzapfel and Ogden, 2017). Further, the effect of the modulus ratio  $r$  on the critical state has been studied extensively for film–substrate bilayers (Cai and Fu, 1999; Hutchinson, 2013; Cai and Fu, 2019; Yin et al., 2018; Alawiye et al., 2019; Nguyen et al., 2020; Liu et al., 2024a), so we no longer repeat the analysis for  $r$  in the current context and will directly focus on the influence of the parameters related to fibers on the critical state.

Fig. 3 shows the critical stretch  $\lambda_{cr}$  and the critical wavenumber  $(kh)_{cr}$  versus fiber stiffness  $k_1$ . The parameter  $r = 0.1$  implies that the HGO film is 10 times stiffer than the neo-Hookean substrate. We select three representative values of the fiber angle, namely  $\theta = 45^\circ, 60^\circ, 90^\circ$ , which implies from Fig. 2 that no fiber is under compression in the homogeneous deformation.

As  $k_1 \rightarrow 0$ , the bilayer structure will reduce to its isotropic counterpart with  $\lambda_{cr} = 0.8947$  and  $(kh)_{cr} = 0.6849$ , regardless of the values of  $\theta$  and  $k_2$ . If  $\theta = 60^\circ$  or  $\theta = 90^\circ$ , the critical stretch  $\lambda_{cr}$  is growing as the fiber stiffness  $k_1$  increases as shown in Fig. 3(a). Therefore, a stiffer fiber will promote surface wrinkling.

However, for  $\theta = 45^\circ$ , a reverse trend is observed. Such non-monotonic characteristic in terms of the fiber angle is typical in fiber-reinforced materials, such as in cylindrical tubes (Goriely and Tabor, 2013) and in a film bonded to an anisotropic substrate (Stewart et al., 2016; Nguyen et al., 2020). In addition, the admissible range of  $\lambda_{cr}$  for  $\theta = 90^\circ$  has the maximum amplitude while the counterpart for  $\theta = 45^\circ$  has the minimum. This implies that the tangent of each curve is also dependent on the fiber angle  $\theta$ . Fig. 3(b) shows the same monotonically decreasing behavior for the critical wavenumber as the fiber stiffness  $k_1$  varies. Consequently, the inclusion of fibers creates a pattern with less wrinkles.

We further show the influence of the fiber angle  $\theta$  from  $0^\circ$  to  $90^\circ$  on the critical state in Fig. 4. The black line corresponds to the isotropic counterpart. It can be seen from Figs. 4(a) and 4(b) that the curves for  $k_1 = 0.1$  and  $0.01$  are similar. In particular, there are two intersection points, marked by  $\theta_{iso}$ , where the critical stretch  $\lambda_{cr}$  is identical to that of the isotropic structure. We further identify the intersections of the blue and red curves with the transition angle  $\theta_{tr}$  illustrated in Fig. 2 and find that  $\theta \approx 42^\circ$  for both curves, which is also close to the local minimum. The dashed part of each curve indicates that the fibers will be compressive for these angles, and as a result has no physical meaning. Moreover, a stable bilayer is attained if  $42^\circ < \theta < \theta_{iso}$ . In this case, the stiffness of the fiber can be used to delay surface instability. Otherwise, anisotropy promotes the instability, and a stiffer fiber will give rise to an earlier instability.

In Fig. 4(b) we show the monotonic nature of the critical wavenumber  $(nh)_{cr}$  as a function of  $\theta$  in the solid curve. In that case, less wrinkles are created with fibers perpendicular to the compression direction (which is expected physically as wrinkles are then more energetically costly to create). A clear feature is that the wavenumber is lower for a higher  $k_1$ , which is consistent with the results illustrated in Fig. 3(b).

In general, the angles  $\theta_{iso}$  and  $\theta_{tr}$  are the solutions of

$$\begin{aligned} \Xi(\lambda_{iso}, (nh)_{iso}, r, k_1, k_2, \theta) &= 0, \\ \Xi(\lambda, nh, r, k_1, k_2, \theta) \Big|_{\lambda = \frac{\sin 2\theta}{1 + \cos 2\theta}} &= 0, \quad \frac{\partial \Xi(\lambda, nh, r, k_1, k_2, \theta)}{\partial (nh)} \Big|_{\lambda = \frac{\sin 2\theta}{1 + \cos 2\theta}} = 0, \end{aligned} \tag{3.21}$$

where the subscript ‘iso’ indicates the corresponding critical stretch and critical wavenumber for the neo-Hookean bilayer counterpart. The associated results are shown in Fig. 5. We highlight different regions by colors to indicate the effect of fiber

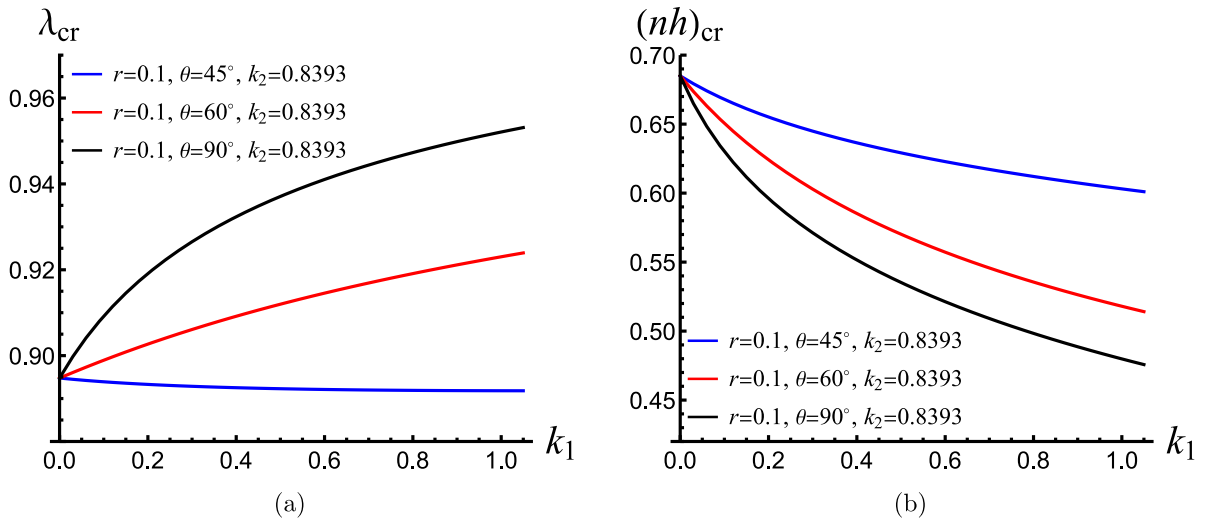


Fig. 3. The critical stretch  $\lambda_{cr}$  and the critical wavenumber  $(nh)_{cr}$  as functions of  $k_1$  when  $r = 0.1$ ,  $k_2 = 0.8393$  with different values of  $\theta$  for an HGO film.

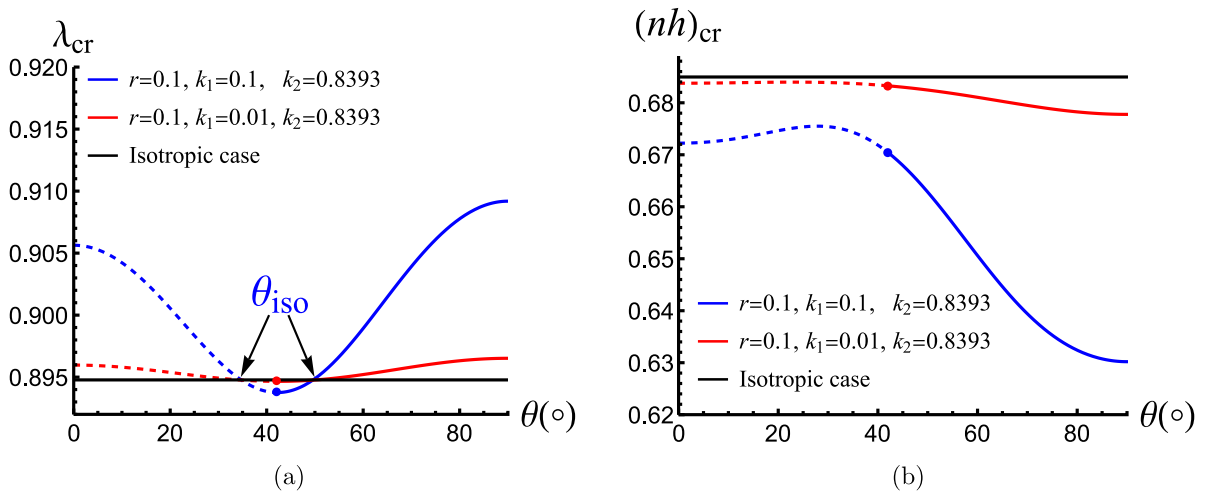


Fig. 4. The critical stretch  $\lambda_{cr}$  and the critical wavenumber  $(nh)_{cr}$  as functions of fiber angle  $\theta$  when  $r = 0.1$ ,  $k_2 = 0.8393$  with different values of  $k_1$  for an HGO film.

reinforcement on the onset of surface instability. We see that the two transition angles  $\theta_{iso}$  and  $\theta_{tr}$  are nearly independent of the fiber stiffness  $k_1$ . However, the value of  $k_1$  will definitely affect the magnitude of the critical stretch away from the isotropic counterpart for a given fiber angle  $\theta$ , as shown in Fig. 4(a). From Fig. 5(b), we observe that the modulus ratio  $r$  has a prominent influence on the lower transition angle  $\theta_{tr}$ . However, the higher transition angle  $\theta_{iso}$  is almost identical as  $r$  changes.

### 3.2. Case II: neo-hookean film/HGO substrate

Next, we assume that the film is isotropic while the substrate is fiber-reinforced. Surface wrinkling of such anisotropic bilayers has been extensively studied through both linear analysis and finite element simulations (Stewart et al., 2016; Nguyen et al., 2020; Guo and Nie, 2023). Previous studies have uncovered fundamental insights into the effects of fiber properties on the critical state. Hence, we only study the dependence of the critical stretch  $\lambda_{cr}$  and the critical wavenumber  $(nh)_{cr}$  on the fiber angle  $\theta$  in Fig. 6.

As shown in Fig. 6, which recovers the results of Stewart et al. (2016) and Nguyen et al. (2020), the critical stretch and wavenumber are non-monotonic with respect to the fiber angle. Comparisons of Figs. 6(a) and 6(b) indicate that the  $\lambda_{cr}$ -curve and the  $(nh)_{cr}$ -curve are almost symmetric. For instance, the two local minima of the red curve in Fig. 6(a) are attained at  $\theta \approx 23.21^\circ$  and  $\theta \approx 68.35^\circ$ , while the red curve in Fig. 6(b) has two local maxima at  $\theta \approx 24^\circ$  and  $\theta \approx 66.91^\circ$ . The dashed lines indicate the angle values that are excluded in the HGO model as the fibers are in compression. Therefore, we consider values of  $\theta$  starting approximately at  $44^\circ$ . Moreover, if the substrate is fiber-reinforced, the critical stretch curve, as shown in Fig. 6(a), is always lower

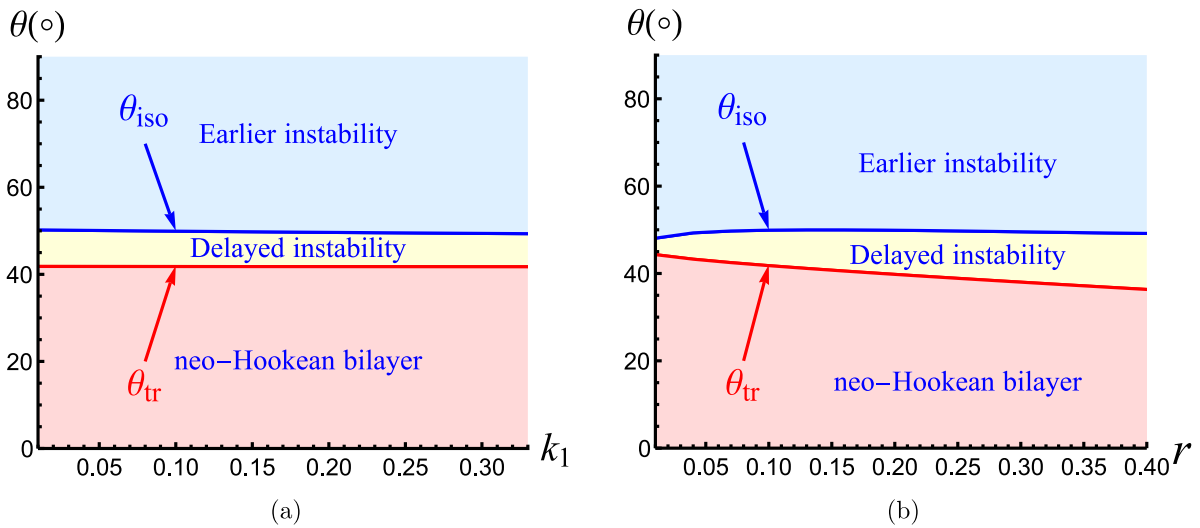


Fig. 5. The transition angles  $\theta_{iso}$  and  $\theta_{tr}$  as functions of  $k_1$  and  $r$ . The parameters are given by  $k_2 = 0.8393$ , (a)  $r = 0.1$  and (b)  $k_1 = 0.1$ . The film is composed of an HGO material.

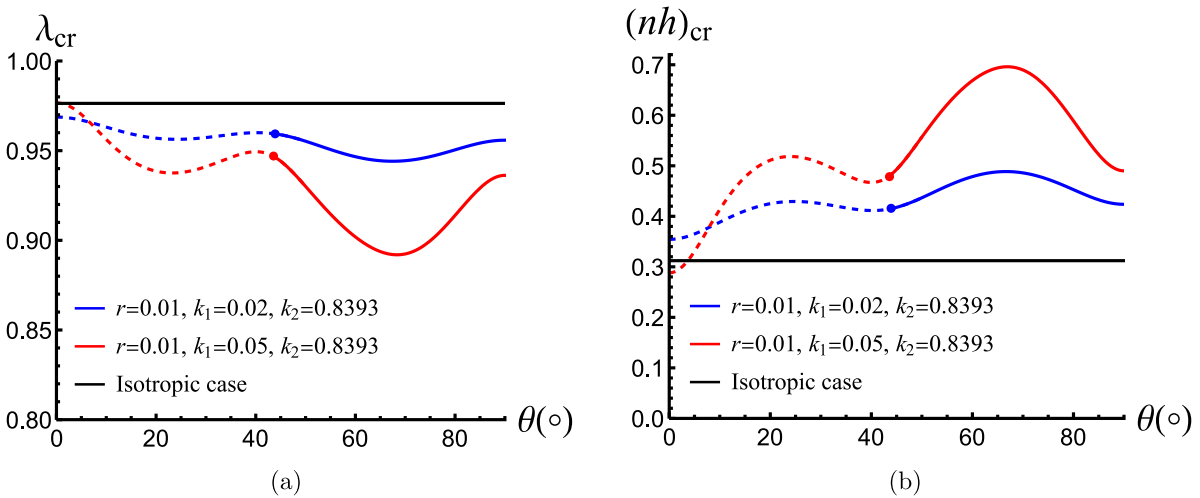


Fig. 6. The critical stretch  $\lambda_{cr}$  and the critical wavenumber  $(nh)_{cr}$  as functions of fiber angle  $\theta$  as  $r = 0.01$ ,  $k_2 = 0.8393$  with different values of  $k_1$ . The substrate is composed of an HGO material. In this case,  $r = 0.01$  and  $k_1 = 0.02$  result in  $\mu_{HGO} = 0.01\mu_{nH}$  and  $k_1 = 0.02\mu_{nH} = 2\mu_{HGO}$ .

than the black line. Similarly, the associated critical wavenumber is higher than the black line. Thus, fiber reinforcement in the substrate *delays the instability and results in more wrinkles*.

In Fig. 6, we focus on the case where  $\mu_{nH}$  is much larger than both  $k_1$  and  $\mu_{HGO}$ . The fibers still have a considerable influence on the critical state. In Fig. 7 we investigate how fiber stiffness and fiber angle affect the bifurcation. We find that the critical stretches for the blue ( $k_1 = 0.07$ ) and red ( $k_1 = 0.1$ ) curves are given by  $\lambda_{cr} \approx 0.7821$  and  $\lambda_{cr} \approx 0.6639$ , respectively. However, when for larger values of  $k_1$  (black curve), the local maximum disappears and instead turns into a local minimum. As a result, the critical stretch is replaced by  $\lambda_{cr} \approx 0.5437$ , which is attained as  $nh \rightarrow \infty$ . This value is the Biot value, originally identified for surface instabilities in a compressed half-space (Biot, 1963). We refer to the instability associated with the Biot value and infinite wavenumber as ‘Biot instability’ to distinguish it from the wrinkling in a bilayer with finite wavenumber. This implies that there exists a special value of  $k_1$ , across which a mode transition between surface wrinkles and Biot instability takes place. We further display the bifurcations when the fiber angle is varying in Fig. 7(b) by taking  $k_1 = 0.12$ . The critical stretches for  $\theta = 80^\circ$  (blue curve) and  $\theta = 60^\circ$  (black curve) are found to be  $\lambda_{cr} \approx 0.6417$  and  $\lambda_{cr} \approx 0.6131$ , respectively. In particular, the black curve ( $\theta = 60^\circ$ ) has two local maxima. A similar phenomenon was reported when a substrate is coated by a double-layer (Zhou et al., 2022).

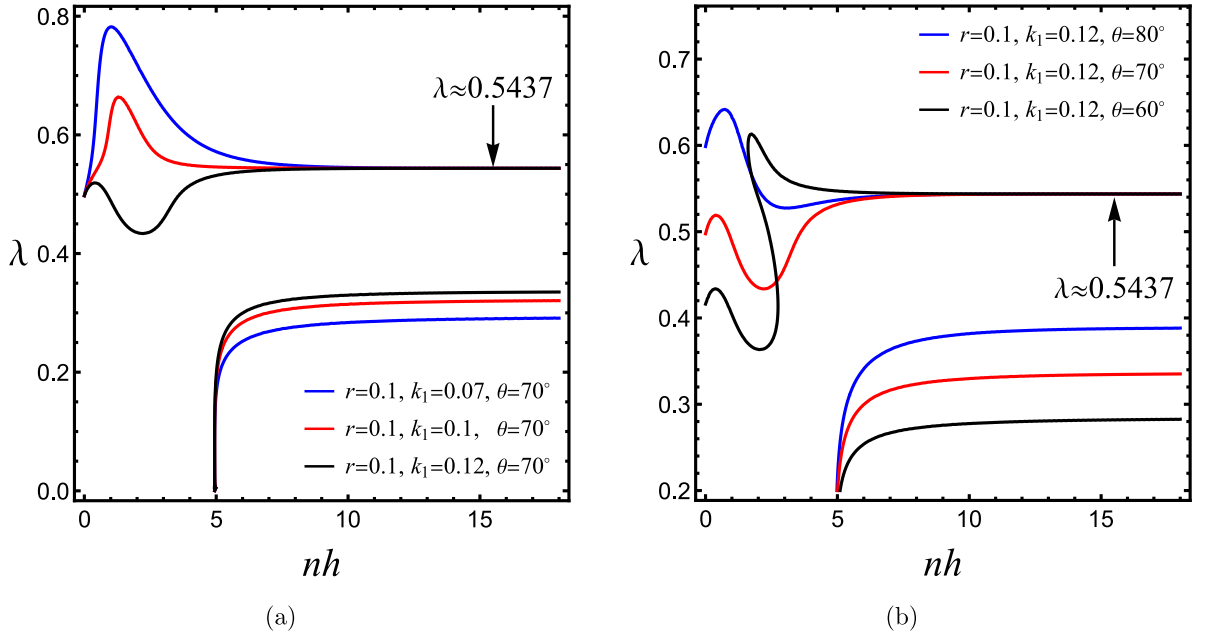


Fig. 7. Bifurcation curves when fiber stiffness  $k_1$  and fiber angle  $\theta$  take different values. The parameter  $k_2$  is specified by 0.

When  $\theta = 70^\circ$ , it is already known from Fig. 7(a) that  $\lambda_{cr} \approx 0.5437$ . Similarly, we know that as the fiber angle decreases from  $\theta = 80^\circ$ , the instability mode changes from surface wrinkling (finite wavenumber) to a Biot instability (infinite wavenumber). As the fiber angle further reduces to  $\theta = 60^\circ$ , the Biot instability will give way to surface wrinkling. These facts indicate the existence of two possible fiber angles where transitions between different modes may occur.

Currently, we have shown that there exist several transition fiber angles, i.e., the angle distinguishing an HGO material and a neo-Hookean material, as shown in Fig. 2, and the angle distinguishing wrinkles and Biot instability, as shown in Fig. 7. The first transition angle can be found in light of (3.21)<sub>2</sub>. For the latter case, we know that there are two angles. The higher one can be found by

$$\Xi(\lambda, nh, r, k_1, k_2, \theta) \Big|_{\lambda=0.5437} = 0, \quad \frac{\partial \Xi(\lambda, nh, r, k_1, k_2, \theta)}{\partial(nh)} \Big|_{\lambda=0.5437} = 0, \quad (3.22)$$

where  $r, k_1, k_2$  are given and  $nh, \theta$  are two unknowns.

However, the solution procedure for small angles is hard to identify numerically, because the maximum of black curve in Fig. 7(b) coincides with the horizontal line  $\lambda \approx 0.5437$  at this transition angle. Correspondingly, there is only one critical wavenumber  $(nh)_{cr} \rightarrow \infty$ , and the second Eq. (3.22)<sub>2</sub> fails. To bypass this difficulty, we approximate the solution by moving the stretch from 0.5437 to  $0.5437 \times 1.01$  (one percent higher) in (3.22). Finally, we express the phase diagrams in Fig. 8. The light blue regions correspond to wrinkles of a bilayer where the substrate is fiber-reinforced. The Biot instability is dominant in the light yellow regions, while the bilayer behaves as a neo-Hookean bilayer in the light red domains. We point out that these phase diagrams are merely based on a linear bifurcation analysis and may be subject to modification when the result of nonlinear analysis is taken into consideration.

#### 4. Weakly nonlinear analysis

A linear bifurcation analysis is essential for understanding pattern formation in soft structures. However, insight into post-buckling evolution can only be extracted in the nonlinear regime.

In this section, we carry out a weakly nonlinear analysis for anisotropic bilayers. Although challenging, a robust theoretical framework in finite elasticity has been established by Ogden (1984). For homogeneous and isotropic bilayers, post-buckling analyses have been conducted by Cai and Fu (1999), Hutchinson (2013), Fu and Ciarletta (2015), Cai and Fu (2019) and Alawiye et al. (2020) for planar structures, and by Jin et al. (2019) and Taffetani and Hennessy (2024) for curved structures.

Similar to the bifurcation analysis, we will elaborate on the solution procedure without distinguishing case I and case II, and only give details for the film where all symbols are presented without hats.

To perform a nonlinear analysis, we assume the following scaling:

$$\lambda = \lambda_{cr} + \varepsilon^2 \lambda_1, \quad \bar{p} = \bar{p}_{cr} + \varepsilon^2 \bar{p}_1, \quad (4.1)$$

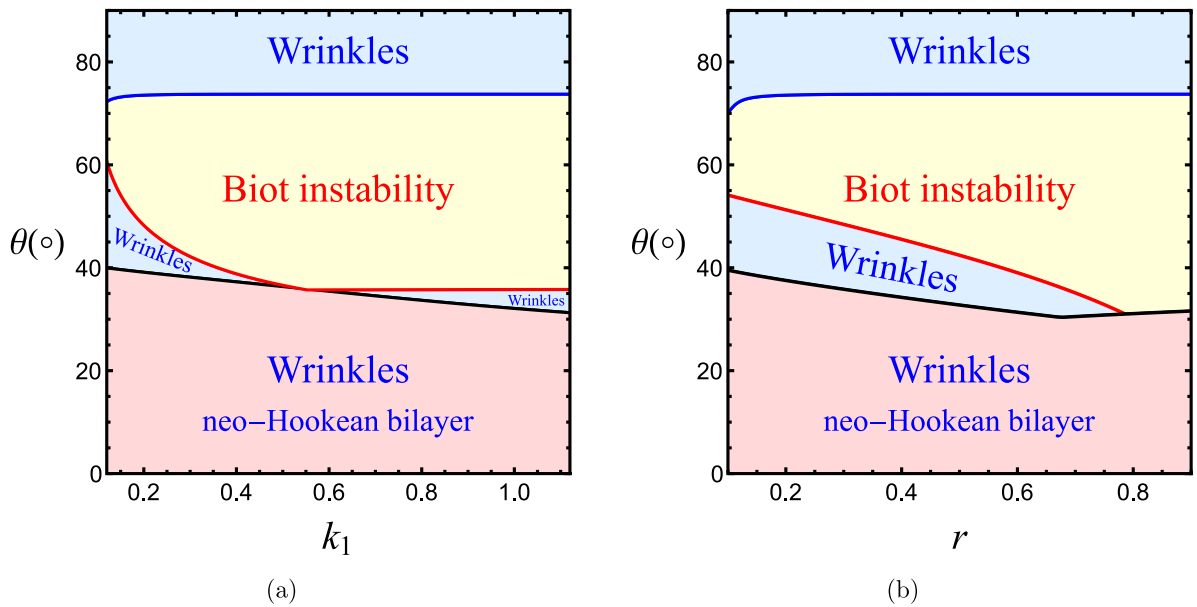


Fig. 8. Phase diagrams of (a) the fiber angle  $\theta$  and fiber stiffness  $k_1$  with  $r = 0.1$ ,  $k_2 = 0$  and (b) the fiber angle  $\theta$  and the modulus ratio  $r$  with  $k_1 = 0.15$ ,  $k_2 = 0$ .

where  $\lambda_{cr}$  is the critical stretch,  $\bar{p}_{cr}$  is the pressure of the critical state,  $\epsilon$  is a small parameter characterizing the magnitude of the incremental displacement, and  $(\lambda_1, \bar{p}_1)$  are constants of  $\mathcal{O}(1)$ . In view of (4.1)<sub>1</sub>, we expand the instantaneous moduli in (2.11) as

$$\begin{aligned} \mathcal{A}_{jilk}^1 &= \mathcal{A}_{jilk}^1 \Big|_{\lambda=\lambda_{cr}} + \epsilon^2 \lambda_1 \mathcal{A}_{jilk}^{1\prime}, \\ \mathcal{A}_{jilknm}^1 &= \mathcal{A}_{jilknm}^1 \Big|_{\lambda=\lambda_{cr}} + \epsilon^2 \lambda_1 \mathcal{A}_{jilknm}^{1\prime}, \\ \mathcal{A}_{jilknmap}^1 &= \mathcal{A}_{jilknmap}^1 \Big|_{\lambda=\lambda_{cr}} + \epsilon^2 \lambda_1 \mathcal{A}_{jilknmap}^{1\prime}, \end{aligned} \tag{4.2}$$

where we have defined

$$\mathcal{A}_{jilk}^{1\prime} = \frac{\partial \mathcal{A}_{jilk}^1}{\partial \lambda} \Big|_{\lambda=\lambda_{cr}}, \quad \mathcal{A}_{jilknm}^{2\prime} = \frac{\partial \mathcal{A}_{jilknm}^2}{\partial \lambda} \Big|_{\lambda=\lambda_{cr}}, \quad \mathcal{A}_{jilknmap}^{3\prime} = \frac{\partial \mathcal{A}_{jilknmap}^3}{\partial \lambda} \Big|_{\lambda=\lambda_{cr}}. \tag{4.3}$$

In the following, we keep the original form  $\mathcal{A}_{jilk}^1$  to denote the associated projection onto  $\lambda = \lambda_{cr}$  for convenience.

We then look for an asymptotic solution of the form

$$\begin{aligned} u_i &= \epsilon u_i^{(1)}(x_1, x_2) + \epsilon^2 u_i^{(2)}(x_1, x_2) + \epsilon^3 u_i^{(3)}(x_1, x_2) + \dots, \\ p^* &= \epsilon p^{(1)}(x_1, x_2) + \epsilon^2 p^{(2)}(x_1, x_2) + \epsilon^3 p^{(3)}(x_1, x_2) + \dots. \end{aligned} \tag{4.4}$$

Inserting (4.4) into (2.12) and (2.13) yields three series equations in  $\epsilon$ . The leading-order equations can be obtained from the coefficients of  $\epsilon$  and it can be readily verified that the resulting system admits the following solutions

$$u_1^{(1)} = A \zeta'(x_2) E + c.c., \quad u_2^{(1)} = -i A \zeta(x_2) E + c.c., \quad p^{(1)} = A P_1 E + c.c., \quad E = e^{ix_1}, \tag{4.5}$$

where a prime is defined as a derivative with respect to  $x_2$ ,  $A$  is the unknown amplitude,  $\zeta$  (and  $\hat{\zeta}$ ) can be found in (3.6), ‘c.c.’ denotes the complex conjugate of the previous term, and  $P_1$  is solved by substituting (4.5) into (3.1)<sub>1</sub> (with  $i = 1$ ):

$$P_1(x_2) = -i \mathcal{A}_{2121}^1 \zeta''' + i (\mathcal{A}_{1111}^1 - \mathcal{A}_{1122}^1 - \mathcal{A}_{1221}^1) \zeta'. \tag{4.6}$$

We set  $n = 1$  without loss of generality as  $h$  and  $n$  always appear in the product  $nh$  and we use  $h$  to obtain different values of  $nh$ . In fact, (4.5) is the solution of the linear bifurcation analysis with an unknown amplitude written as  $A$ .

The coefficients of  $\epsilon^2$  provide

$$\begin{aligned} u_{1,1}^{(2)} + u_{2,2}^{(2)} &= \frac{1}{2} u_{i,j}^{(1)} u_{j,i}^{(1)}, \\ \mathcal{A}_{jilk}^1 u_{k,lj}^{(2)} - p_{,i}^{(2)} &= -\mathcal{A}_{jilknm}^2 u_{m,n}^{(1)} u_{k,lj}^{(1)} - p_{,j}^{(1)} u_{j,i}^{(1)}, \quad i = 1, 2, \end{aligned} \tag{4.7}$$

along with the boundary conditions and the continuity conditions

$$\left. \begin{aligned} T_i^{(2)} &= 0, & \text{on } x_2 = h, \\ u_i^{(2)} &= \hat{u}_i^{(2)}, \quad T_i^{(2)} = \hat{T}_i^{(2)}, & \text{on } x_2 = 0, \\ \hat{u}_i^{(2)} &\rightarrow 0, & \text{as } x_2 \rightarrow -\infty, \end{aligned} \right\} \quad i = 1, 2, \tag{4.8}$$

where

$$T_i^{(2)} = \mathcal{A}_{2ilk}^1 u_{k,l}^{(2)} + \bar{p}_{cr} u_{2,i}^{(2)} - p^{(2)} \delta_{2i} + \frac{1}{2} \mathcal{A}_{2ilknm}^2 u_{k,l}^{(1)} u_{m,n}^{(1)} - \bar{p}_{cr} u_{2,k}^{(1)} u_{k,i}^{(1)} + p^{(1)} u_{2,i}^{(1)}. \tag{4.9}$$

In particular, the inhomogeneous terms are related to

$$u_{i,j}^{(1)} = A \Gamma_{ij}^{(1)} E + \text{c.c.}, \tag{4.10}$$

with

$$\Gamma_{11}^{(1)} = i\zeta', \quad \Gamma_{12}^{(1)} = \zeta'', \quad \Gamma_{21}^{(1)} = \zeta, \quad \Gamma_{22}^{(1)} = -i\zeta'. \tag{4.11}$$

It can be readily checked that the inhomogeneous terms in (4.7) are linear combinations of  $E^0$ ,  $E^2$ , and  $E^{-2}$ . Therefore, we are able to pursue a particular solution for  $(u_1^{(2)}, u_2^{(2)}, p^{(2)})$  as

$$\begin{aligned} u_1^{(2)} &= AA^* U_0(x_2) + A^2 U_2(x_2) E^2 + \text{c.c.}, \\ u_2^{(2)} &= AA^* V_0(x_2) + A^2 V_2(x_2) E^2 + \text{c.c.}, \\ p^{(2)} &= AA^* P_0 + A^2 P_2 E^2 + \text{c.c.}, \end{aligned} \tag{4.12}$$

where the \* denotes the complex conjugate.

To identify the unknown functions  $U_0, U_2, V_0, V_2, P_0, P_2$ , we substitute (4.12) into (4.7), (4.8) and collect the coefficients of  $E^0$  and  $E^2$ . As a result, a well-imposed equation system is obtained. Specifically, many of them can be solved directly to give rise to analytical expressions of  $U_0, U_2, V_0, P_0$ , and  $P_2$ , and  $V_2$  satisfies the following equation

$$\mathcal{A}_{2121}^1 V_2'''' - 4(\mathcal{A}_{1111}^1 + \mathcal{A}_{2222}^1 - 2\mathcal{A}_{1122}^1 - 2\mathcal{A}_{1221}^1) V_2'' + 16\mathcal{A}_{1212}^1 V_2 = \Phi(x_2), \tag{4.13}$$

where  $\Phi(x_2)$  is related to  $\mathcal{A}_{jilknm}^2 \zeta(x_2)$  and its derivatives, and the long expression is omitted for brevity. After some manipulations we recast (4.13) as

$$V_2'''' - (1 + \tau^2) \alpha^2 V_2'' + \tau^2 \alpha^4 V_2 = \phi(x_2). \tag{4.14}$$

Note that  $\phi = \Phi/\mathcal{A}_{2121}^1$  and we have denoted the square of eigenvalues of the homogeneous part of (4.13) by  $\alpha^2$  and  $\alpha^2 \tau^2$ , respectively.

A particular solution of (4.14) can be obtained by using Laplace transforms (Fu and Cai, 2015):

$$\begin{aligned} V_{PS} &= \frac{1}{2\alpha^3 \tau (1 - \tau^2)} \left\{ \tau e^{\alpha x_2} \int_0^{x_2} e^{-at} \phi(t) dt - e^{\alpha \tau x_2} \int_0^{x_2} e^{-\alpha \tau t} \phi(t) dt \right. \\ &\quad \left. + e^{-\alpha \tau x_2} \int_{-\infty}^{x_2} e^{\alpha \tau t} \phi(t) dt - \tau e^{-\alpha x_2} \int_{-\infty}^{x_2} e^{\alpha t} \phi(t) dt \right\}. \end{aligned} \tag{4.15}$$

Laplace transforms are not applicable to the layer. Alternatively, the method of variation of parameters can be applied. It is found that by simply changing the lower limit from  $\infty$  to 0 in the particular integral of (4.15), the same expression as that derived from the variation of parameters method can be obtained. Ultimately, the general solution of  $V_2$  can be written as

$$V_2(x_2) = d_1 e^{\alpha x_2} + d_2 e^{\alpha \tau x_2} + d_3 e^{-\alpha x_2} + d_4 e^{-\alpha \tau x_2} + V_{PS}, \tag{4.16}$$

where  $d_i$  ( $i = 1, 2, 3, 4$ ) are constants to be determined from the boundary conditions and  $\alpha, \alpha \tau$  take the positive real parts. For the half-space,  $d_3$  and  $d_4$  must vanish according to the decaying condition at infinity.

With the use of (4.12)<sub>1,2</sub>, we obtain

$$u_{i,j}^{(2)} = AA^* \Gamma_{ij}^{(m)} + A^2 \Gamma_{ij}^{(2)} E^2 + \text{c.c.}, \tag{4.17}$$

where

$$\begin{aligned} \Gamma_{11}^{(m)} &= 0, \quad \Gamma_{12}^{(m)} = U_0', \quad \Gamma_{21}^{(m)} = 0, \quad \Gamma_{22}^{(m)} = V_0', \\ \Gamma_{11}^{(2)} &= 2iU_2, \quad \Gamma_{12}^{(2)} = U_2', \quad \Gamma_{21}^{(2)} = 2iV_2', \quad \Gamma_{22}^{(2)} = V_2'. \end{aligned} \tag{4.18}$$

For the neo-Hookean model, we are able to write explicitly the solutions as

$$\begin{aligned} U_0 &= 0, \quad V_0 = 2\zeta\zeta', \quad P_0 = 2\mu_{nH} \lambda_{cr}^{-2} (\zeta\zeta')' + 2iP_1\zeta', \\ 2iU_2 &= -V_2' + \zeta\zeta'' - \zeta'^2, \quad 2iP_2 = \mu_{nH} \lambda_{cr}^{-2} U_2'' - 4\mu_{nH} \lambda_{cr}^2 U_2 + P_1'\zeta - P_1\zeta', \\ V_{PS} &= \frac{\lambda_{cr}^4 - 1}{9\lambda^8 - 82\lambda^4 + 9} (9\zeta\zeta''' - 21\zeta'\zeta''). \end{aligned} \tag{4.19}$$

However, for the HGO model, the counterparts are lengthy and hence are omitted here.

At this point, we are in a position to determine the unknown amplitude  $A$ . To achieve this, we refer to the methodology proposed by Fu (1995) and Fu and Devenish (1996) and employ the principle of virtual work

$$\int_{-\infty}^h \int_0^{2\pi} \chi_{ij} u_{i,j}^{\circ} dx_1 dx_2 = 0, \tag{4.20}$$

where  $u_i^{\circ}$  corresponds to the linear solutions with  $n = -1$  and precisely possesses the form of

$$\begin{aligned} u_1^{\circ} &= \zeta' (x_2) e^{-ix_1}, & u_2^{\circ} &= i\zeta (x_2) e^{-ix_1}, & 0 \leq x_2 \leq h, \\ \hat{u}_1^{\circ} &= \hat{\zeta}' (x_2) e^{-ix_1}, & \hat{u}_2^{\circ} &= i\hat{\zeta} (x_2) e^{-ix_1}, & -\infty < x_2 \leq 0. \end{aligned} \tag{4.21}$$

It is again emphasized that when an integration is carried out within the region occupied by the substrate a hat will be added on the corresponding quantity. We, however, disregard hats in illustrating the derivation of amplitude equation for simplicity, as seen in (4.20).

On substituting (4.4) into (2.10) and then inserting the resulting expression into (4.20), we can collect the coefficients of  $\epsilon$ ,  $\epsilon^2$ , and  $\epsilon^3$ . It is found that the first two equations by equating the coefficients of  $\epsilon$  and  $\epsilon^2$  to zeros are automatically true. The coefficient of  $\epsilon^3$  leads to

$$\int_{-\infty}^h \int_0^{2\pi} \left\{ \left( \mathcal{A}_{jilk}^1 u_{k,l}^{(3)} + \bar{p}_{cr} u_{j,i}^{(3)} - p^{(3)} \delta_{ji} + \bar{p}_1 u_{j,i}^{(1)} + \lambda_1 \mathcal{A}_{jilk}^1 u_{k,l}^{(1)} + \sigma_{ij}^{(3)} \right) u_{i,j}^{\circ} \right\} dx_1 dx_2 = 0, \tag{4.22}$$

where

$$\sigma_{ij}^{(3)} = \mathcal{A}_{jilknm}^2 u_{k,l}^{(1)} u_{m,n}^{(2)} + \frac{1}{6} \mathcal{A}_{jilkmp}^3 u_{k,l}^{(1)} u_{m,n}^{(1)} u_{p,q}^{(1)} + p^{(1)} u_{j,i}^{(2)} + p^{(2)} u_{j,i}^{(1)}. \tag{4.23}$$

Our next step is to eliminate  $u_i^{(3)}$  and  $p^{(3)}$  in (4.22). For this purpose, we repeatedly use integration by parts for terms containing  $u_i^{(3)}$  and  $p^{(3)}$  based on the fact that  $u_i^{\circ}$  is a linear solution and by means of the identity obtained from the coefficients of  $\epsilon^3$  of (2.13), namely,

$$u_{i,i}^{(3)} = u_{i,j}^{(1)} u_{j,i}^{(2)}. \tag{4.24}$$

After some manipulations, we arrive at

$$\int_{-\infty}^h \int_0^{2\pi} \left\{ \bar{p}_1 u_{j,i}^{(1)} u_{i,j}^{\circ} + \lambda_1 \mathcal{A}_{jilk}^1 u_{k,l}^{(1)} u_{i,j}^{\circ} + p^{\circ} u_{i,j}^{(1)} u_{j,i}^{(2)} + \sigma_{ij}^{(3)} u_{i,j}^{\circ} \right\} dx_1 dx_2 = 0. \tag{4.25}$$

where the pressure field  $p^{\circ}$  is associated with  $u_i^{\circ}$  and is given by

$$p^{\circ} = [i\mathcal{A}_{2121}^1 \zeta''' - i(\mathcal{A}_{1111}^1 - \mathcal{A}_{1122}^1 - \mathcal{A}_{1221}^1) \zeta'] e^{-ix_1}. \tag{4.26}$$

Substituting (4.5)<sub>3</sub>, (4.10), (4.12)<sub>3</sub> and (4.17) into (4.25), making use of the fact that  $u_{i,j}^{\circ} = \Gamma_{ij}^{(1)*} E^{-1}$ , and computing the integral over  $x_1$ , we deduce the amplitude equation

$$c_{01} \lambda_1 A + c_{03} |A|^2 A = 0, \tag{4.27}$$

where  $c_{01}$  and  $c_{03}$  take the following forms:

$$c_{01} = \int_{-\infty}^h \left\{ \mathcal{A}_{jilk}^1 \Gamma_{kl}^{(1)} \Gamma_{ji}^{(1)*} + \frac{P_1}{\lambda_1} \Gamma_{ij}^{(1)} \Gamma_{ji}^{(1)*} \right\} dx_2, \tag{4.28}$$

$$c_{03} = \int_{-\infty}^h \left\{ P_1^* \left( \Gamma_{ij}^{(1)} \Gamma_{ji}^{(m)} + 2\Gamma_{ij}^{(1)*} \Gamma_{ji}^{(2)} \right) + K_{ij} \Gamma_{ij}^{(1)*} \right\} dx_2,$$

with

$$K_{ij} = \mathcal{A}_{jilknm}^2 \left( \Gamma_{kl}^{(1)} \Gamma_{mn}^{(m)} + \Gamma_{kl}^{(1)*} \Gamma_{mn}^{(2)} \right) + \frac{1}{2} \mathcal{A}_{jilkmp}^3 \Gamma_{kl}^{(1)*} \Gamma_{mn}^{(1)} \Gamma_{pq}^{(1)} + P_1 \Gamma_{ji}^{(m)} + P_0 \Gamma_{ji}^{(1)} + P_2 \Gamma_{ji}^{(1)*}. \tag{4.29}$$

Eq. (4.27) admits a non-trivial solution:

$$|A|^2 = -\frac{\lambda_1}{c_1}, \quad \text{with } c_1 \equiv \frac{c_{03}}{c_{01}}, \tag{4.30}$$

which determines the nonlinear evolution of the amplitude  $A$  for a given mode  $nh$ .

The amplitude equation presented above has a rational solution if and only if the ratio  $\lambda_1/c_1$  is negative. This condition establishes the criterion to determine the bifurcation nature: the bifurcation is *supercritical* when  $c_1$  is positive and *subcritical* otherwise (Hutchinson and Koiter, 1970). In the subsequent analysis, we consider the two situations separately to study the transition between supercritical and subcritical bifurcations based on (4.28).

Bearing in mind that the parameter  $k_2$  has a minor impact on the critical state according to the linear bifurcation analysis, we fix  $k_2 = 0$  in the subsequent analysis. As a result, the reduced strain energy form of (3.12) reads

$$W_{\text{HGO}} = \frac{\mu_{\text{HGO}}}{2} (I_1 - 3) + \frac{k_1}{2} \left( (I_4 - 1)^2 + (I_6 - 1)^2 \right). \tag{4.31}$$

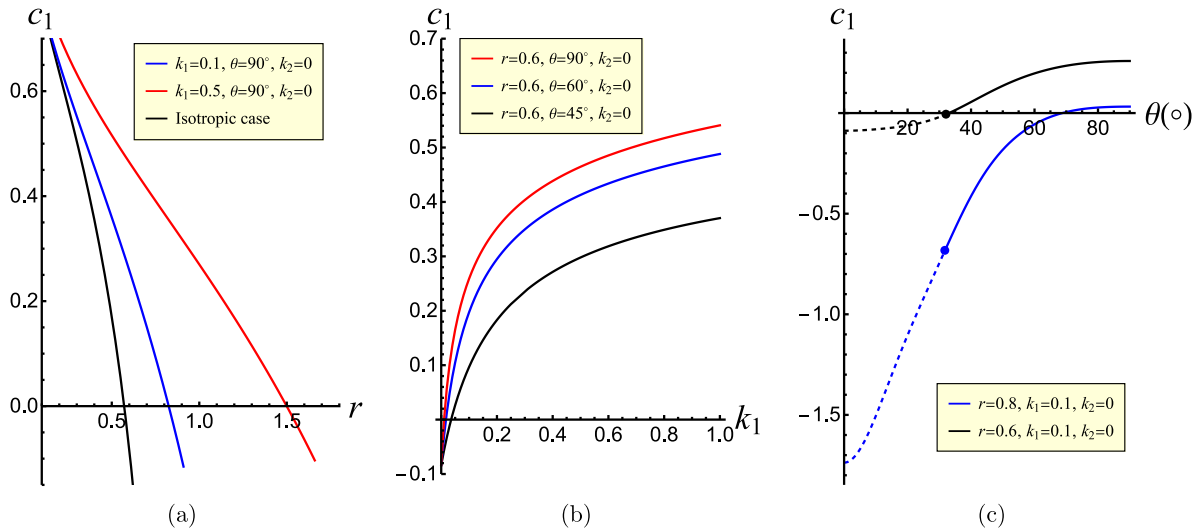


Fig. 9. Dependence of the coefficient  $c_1$  on (a) the modulus ratio  $r$ , (b) the fiber stiffness  $k_1$ , and (c) the fiber angle  $\theta$ . The film is fiber-reinforced and the substrate is isotropic. All used parameters are depicted in each figure.

4.1. Case I: HGO film/neo-Hookean substrate

For an anisotropic film, in Fig. 9 we show the coefficient  $c_1$  against various parameters. For comparison, the isotropic structure is also shown (black curve). In each curve, the zero corresponds to the transition between supercritical bifurcation ( $c_1 > 0$ ) and subcritical bifurcation ( $c_1 < 0$ ). For the isotropic case, this transition happens when  $r \approx 0.571$  (Alawiye et al., 2020). As  $k_1$  increases, this critical transition value increases. For instance, the zero for  $k_1 = 0.1$  is at  $r \approx 0.825$  (blue curve) and at  $r \approx 1.499$  for  $k_1 = 0.5$  (red curve). We infer that increased fiber stiffness will result in a larger transition modulus ratio.

To further confirm the above conclusion, we show the results of  $c_1$  as  $k_1$  varies in Fig. 9(b) where  $r = 0.6$  and  $\theta$  takes the values  $45^\circ, 60^\circ, 90^\circ$ . It can be seen that all curves start from the same point  $c_1 = -0.0836$  when  $k_1 = 0$ , corresponding to the isotropic case, and increase monotonically. Therefore, for  $r = 0.6 > 0.571$ , initially the bifurcation is subcritical and with increased fiber stiffness the subcritical bifurcation is replaced by a supercritical bifurcation. The monotonic function in  $k_1$  implies that  $c_1$  reaches a minimum at  $k_1 = 0$ , regardless of the fiber angle  $\theta$ . We conclude that  $r \approx 0.571$  is a lower bound of the transition value of  $r$  and a subcritical bifurcation is impossible for  $r < 0.571$ .

Fig. 9(c) shows the variation of the coefficient  $c_1$  as a function of the fiber angle  $\theta$ . The dashed curves represent the regime in which fibers are under compression in a homogeneous deformation and are thus excluded from our analysis. The blue and black points correspond to  $\theta \approx 32^\circ$ . Interestingly, each solid curve increases monotonically with respect to  $\theta$ . Originally,  $c_1$  is negative for both cases, resulting in a subcritical bifurcation. As  $\theta$  increases, there is a transition from a subcritical to a supercritical bifurcation.

We define  $r_{tr}$  as the critical value of  $r$  at which a transition from supercritical bifurcation to subcritical occurs, and plot the dependence of  $r_{tr}$  on the fiber stiffness  $k_1$  for  $\theta = 45^\circ, 60^\circ$ , and  $90^\circ$  in Fig. 10. As  $k_1 \rightarrow 0$ , all curves intersect at  $r_{th} \approx 0.571$ . When the fiber orientation is fixed, a subcritical bifurcation, which is sensitive to any imperfection, can occur when the modulus ratio  $r$  is above  $r_{tr}$ . Otherwise, a supercritical bifurcation will be triggered at a critical load. We find that the black curve ( $\theta = 45^\circ$ ) is always lower than other two curves. The red ( $\theta = 90^\circ$ ) curve is initially a little bit higher than the blue one ( $\theta = 60^\circ$ ) until  $k_1 = 0.303941$ . After that, the blue curve becomes higher.

As expected, all curves are monotonically increasing as a function of  $k_1$  (see Fig. 10). This is due to the fact that the film is fiber-reinforced and an increase in the fiber stiffness is equivalent to stiffening the film. For this reason, the single modulus ratio  $r = \mu_{nH}/\mu_{HGO}$  loses its physical relevance. Naturally, both the fiber angle  $\theta$  and the fiber stiffness will be involved in an effective modulus ratio  $\bar{r}$ . To identify this, we look at the stress-strain solution in the homogeneous deformation and calculate the limit when  $\lambda \rightarrow 1$  to obtain the effective shear modulus:

$$\mu_{eff} = \mu_{HGO} + k_1 (1 + \cos 4\theta). \tag{4.32}$$

Since the reduced strain energy function (4.31) is adopted, the parameter  $k_2$  does not appear in the above expression. Note that in this formulation,  $k_1$  retains its original unit of stress. For  $\theta = 90^\circ$ , we find  $\mu_{eff} = \mu_{HGO} + 2k_1$ , whereas for  $\theta = 45^\circ$ , we have  $\mu_{eff} = \mu_{HGO}$ . It follows from (4.31) that, for fixed  $\mu_{HGO}$  and  $k_1$ , increasing  $\theta$  from  $45^\circ$  to  $90^\circ$  leads to a larger value of  $1 + \cos 4\theta$ , thereby stiffening the film. This, in turn, results in an earlier onset of wrinkling instability with fewer wrinkles, which qualitatively explains the results shown in Fig. 4. We therefore define an effective modulus ratio as

$$\bar{r} = \frac{\mu_{nH}}{\mu_{eff}} = \frac{r}{1 + k_1 (1 + \cos 4\theta)}. \tag{4.33}$$

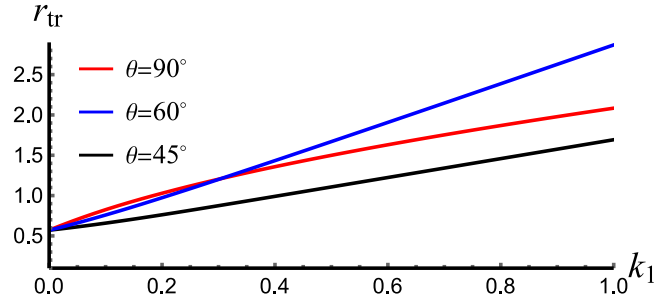


Fig. 10. Dependence of the transition value  $r_{tr}$  on the fiber stiffness  $k_1$  with different fiber angles. The film is fiber-reinforced while the substrate is isotropic.

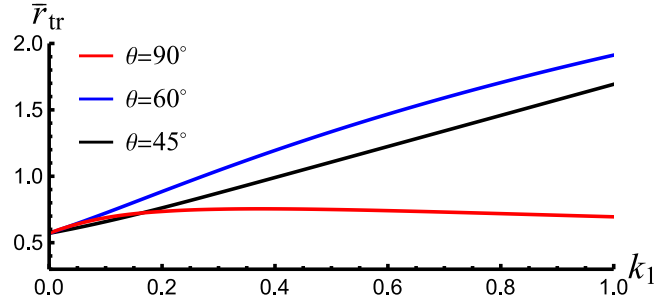


Fig. 11. Dependence of the modified transition value  $\bar{r}_{tr}$  on the fiber stiffness  $k_1$  with different fiber angles. The film is fiber-reinforced while the substrate is isotropic.

By using this new ratio, we plot again Fig. 10 in Fig. 11. It can be seen that the red curve ( $\theta = 90^\circ$ ) approaches 0.571 with an almost uniform correction as  $k_1$  increases. This confirms that the effective modulus (4.32) performs well in this special fiber orientation. However, (4.32) is not adequate to fully capture the combined effects of  $\theta$  and  $k_1$ , as the curves associated with  $\theta = 45^\circ$  and  $\theta = 90^\circ$  still show noticeable deviations from 0.571.

We emphasize that the near-critical evolution of surface wrinkles can be determined from our analytical solution. Obviously, the post-buckling deformation is also involved with the deformation of fibers. Therefore, either compression or tension may be possible for fibers. To investigate this, we refer to (2.3), (3.13), and (3.14) to write

$$I_4 = \frac{\lambda_{cr}^2}{2} \left( (u_{1,1} + 1)^2 + u_{2,1}^2 \right) (1 + \cos 2\theta) + \frac{1}{2\lambda_{cr}^2} \left( (u_{2,2} + 1)^2 + u_{1,2}^2 \right) (1 - \cos 2\theta) + (u_{1,2} + u_{2,1} + u_{1,1}u_{1,2} + u_{2,1}u_{2,2}) \sin 2\theta, \tag{4.34}$$

$$I_6 = \frac{\lambda_{cr}^2}{2} \left( (u_{1,1} + 1)^2 + u_{2,1}^2 \right) (1 + \cos 2\theta) + \frac{1}{2\lambda_{cr}^2} \left( (u_{2,2} + 1)^2 + u_{1,2}^2 \right) (1 - \cos 2\theta) - (u_{1,2} + u_{2,1} + u_{1,1}u_{1,2} + u_{2,1}u_{2,2}) \sin 2\theta, \tag{4.35}$$

where we have defined  $u_{1,1} = \partial u_1 / \partial x_1$ ,  $u_{1,2} = \partial u_1 / \partial x_2$ , etc. Furthermore, we substitute the displacement  $u_i$  ( $i = 1, 2$ ) by the leading-order counterparts  $\epsilon u_i^{(1)}$  and absorb the small parameter  $\epsilon$  into the amplitude  $A$  according to

$$\epsilon |A| = \sqrt{\frac{\lambda_{cr} - \lambda}{c_1}}. \tag{4.36}$$

Consequently, we are able to characterize  $I_4$  and  $I_6$  in the post-buckling regime.

When the fiber angle is  $\theta = 90^\circ$ , it can be deduced from (4.34) and (4.35) that  $I_4 = I_6 = \left( (u_{2,2} + 1)^2 + u_{1,2}^2 \right) / \lambda_{cr}^2$ . Taking  $r = 0.01$  and  $k_1 = 0.5$ , we determine  $\lambda_{cr} = 0.9852$ ,  $(nh)_{cr} = 0.2476$  and  $c_1 = 0.9595$ . Note that in our post-buckling analysis the wavenumber has been chosen by  $n = 1$  without loss of generality. So actually the minimum period of the post-buckling solution is  $2\pi$ . For a given compressive stretch  $\lambda < \lambda_{cr}$ , we define the function

$$I(x_1, x_2) = I_4 - 1 = \frac{\left( u_{2,2}^{(1)} + 1 \right)^2 + \left( u_{1,2}^{(1)} \right)^2}{\lambda_{cr}^2} - 1, \tag{4.37}$$

and find that it attains the same minimum at  $(0, h)$  or  $(2\pi, h)$  within the period  $[0, 2\pi] \times [0, h]$ . Additionally, we ascertain that once  $\lambda_{cr} - \lambda = 0.00365$ , the fibers begin to experience compression. Therefore, we define an admissible domain where post-buckling

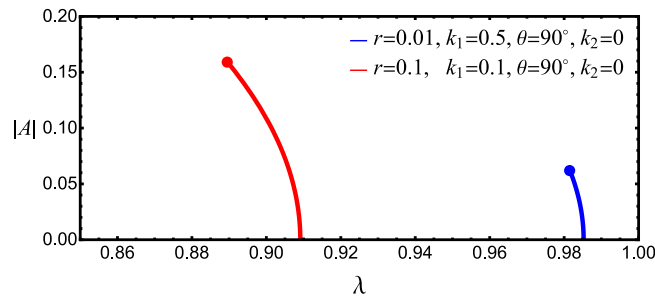


Fig. 12. Bifurcation diagrams based on the post-buckling solution derived in this section when the film is fiber-reinforced. Pitchfork supercritical bifurcations are found for both scenarios.

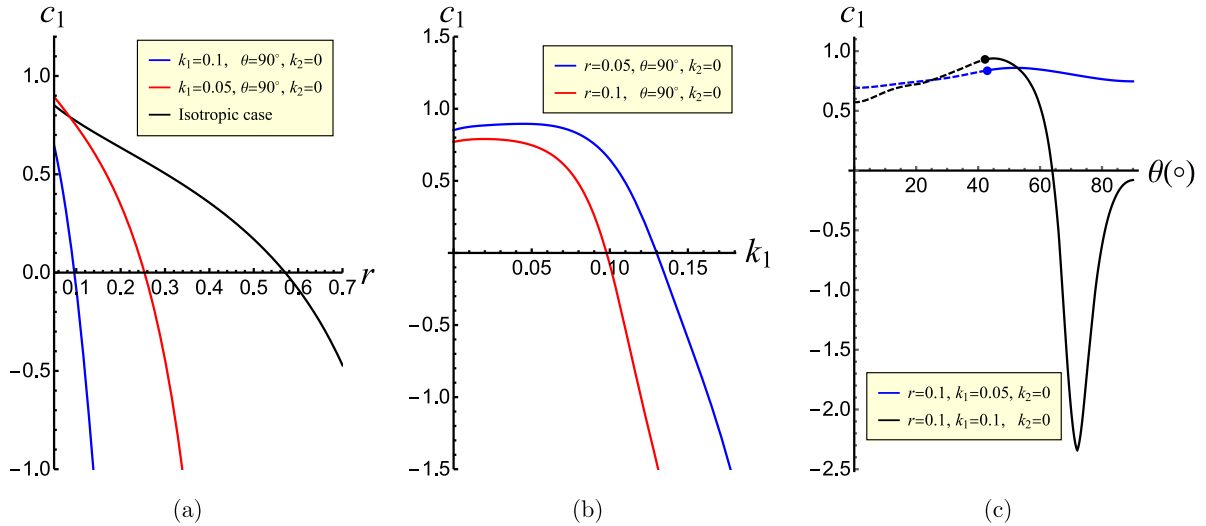


Fig. 13. Dependence of the coefficient  $c_1$  on (a) the modulus ratio  $r$ , (b) the fiber stiffness  $k_1$ , and (c) the fiber angle  $\theta$ . The film is isotropic and the substrate is fiber-reinforced. All used parameters are depicted in each figure.

evolution using HGO model is valid. We further consider  $r = 0.1$  and  $k_1 = 0.1$ . In this scenario, we identify  $\lambda_{cr} = 0.9091$ ,  $(nh)_{cr} = 0.6347$  and  $c_1 = 0.7723$ . By using a similar procedure, we find that the condition where fibers start to undergo compression is given by  $\lambda_{cr} - \lambda = 0.01962$ .

Finally, we present the associated bifurcation diagrams for these two cases in Fig. 12. The blue curve corresponds to  $r = 0.01$  and  $k_1 = 0.5$  while the red curve represents  $r = 0.1$  and  $k_1 = 0.1$ . Compressive loading begins at  $\lambda = 1$  and initially the structure undergoes homogeneous deformation, resulting in a trivial amplitude. When compression reaches the critical value  $\lambda_{cr}$ , where the curve intersects the horizontal axis, bifurcation occurs and triggers surface wrinkling. As the structure is further compressed, the amplitude increases, following the path shown in the figure. We also highlight the endpoints where fibers begin to experience compression, marking the limits where the current post-buckling solution becomes invalid. We conclude that the fibers experience compression earlier if they are stiffer.

4.2. Case II: neo-Hookean film/HGO substrate

For an anisotropic substrate, we use the same post-buckling solution and plot the coefficient  $c_1$  against multiple parameters in Fig. 13. As before, the intersections with the horizontal axis represent the transition between supercritical and subcritical bifurcations. For  $k = 0$  (black curve), which corresponds to an isotropic bilayer, we already know that the zero is  $r \approx 0.571$ . The zeros for  $k_1 = 0.05$  (red curve) and  $k_1 = 0.1$  (blue curve) are found to be  $r \approx 0.254$  and  $r \approx 0.096$ , respectively. Therefore, a stiffer fiber corresponds to a lower transition modulus ratio, exhibiting a behavior that contrasts with the previous case. When  $r \sim 0.1$ , the black curve intersects with the red one, indicating the non-monotonic characteristic of  $c_1$  as a function of  $k_1$ .

To clarify the influence of  $k_1$ , we fix  $r$  and  $\theta = 90^\circ$  in Fig. 13(b). Since the modulus ratios differ for the two curves, they start at different values of  $c_1$  when  $k_1 = 0$ . As expected, both curves slowly rise and then suddenly drop. For  $r = 0.05$  (blue curve), the supercritical bifurcation gives way to the subcritical one when  $k_1 \approx 0.13$ . However, the transition value for  $r = 0.1$  (red curve) occurs at  $k_1 \approx 0.098$ . This manifests that stiffer fibers are needed to induce subcritical bifurcation if the neo-Hookean film is also stiffer.

**Table 1**  
Some values of  $r_{tr}$  where transition between supercritical and subcritical bifurcations takes place for given  $k_1$  and  $\theta = 90^\circ$ .

$k_1$	0.04	0.07	0.1	0.18
$r_{tr}$	0.3020	0.1753	0.0957	0.0144

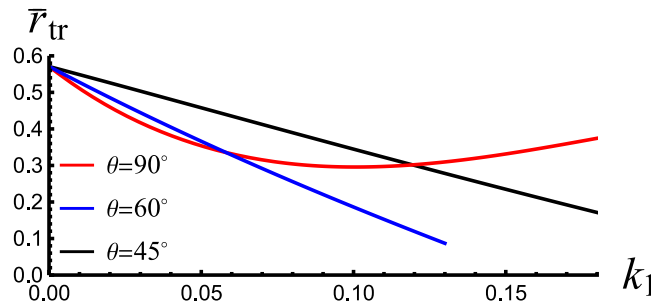


**Fig. 14.** Dependence of the modified transition value  $\bar{r}_{tr}$  on the fiber stiffness  $k_1$  with different fiber angles. The substrate is fiber-reinforced while the film is isotropic.

Fig. 13(c) depicts the relation of  $c_1$  and the fiber angle  $\theta$ . The dashed curve represents fibers under compression and is therefore excluded. If  $k_1 = 0.05$ , the effective angle starts at  $\theta \approx 43^\circ$  and the dependence of  $c_1$  on  $\theta$  is non-monotonic with  $\theta = 90^\circ$  corresponding to a local minimum. Meanwhile, the bifurcation is always supercritical. Nonetheless, when the fiber stiffness increases to  $k_1 = 0.1$ , the effective angle starts from  $\theta \approx 42^\circ$  and the coefficient  $c_1$  varies more significantly with regard to  $\theta$ . Notably, there exists a transition angle at  $\theta \approx 64^\circ$  where the bifurcation shifts from supercritical to subcritical. Additionally, the curve reaches a minimum at  $\theta \approx 72^\circ$  and the tangent around this point is quite sharp.

From the above analysis, we conclude that for  $r > 0.571$  a subcritical bifurcation takes place when the substrate is fiber-reinforced and representative transition modulus ratios are given in Table 1. As expected, with increasing fiber stiffness, the bilayer experiences a subcritical bifurcation at a lower modulus ratio. Specifically, when  $k_1 = 0.18$  the bifurcation is subcritical even for  $r = 0.015$ . In this case, we know  $\mu_{nH} = 66.7\mu_{HGO}$  and  $k_1 = 12\mu_{HGO}$  so it can be seen that the fiber stiffness is dominant in the strain energy function (4.31). Therefore, the shear modulus ratio is not an adequate representation of the stiffness mismatch between the two layers.

To study the combined contribution of the shear modulus of the matrix and the fiber stiffness to the effective substrate stiffness, we use the effective shear modulus (4.32) and define the effective modulus ratio as:

$$\bar{r} = \frac{\mu_{eff}}{\mu_{nH}} = r + k_1 (1 + \cos 4\theta). \tag{4.38}$$

We show the modified transition value  $\bar{r}_{tr}$  versus the fiber stiffness  $k_1$  for  $\theta = 90^\circ, 60^\circ$ , and  $45^\circ$  in Fig. 14. We see that the red curve ( $\theta = 90^\circ$ ) is non-monotonic and deviates significantly from the typical value  $r = 0.571$ . In contrast, the black ( $\theta = 45^\circ$ ) and blue ( $\theta = 60^\circ$ ) curves exhibit monotonic decrease. Specifically, the blue curve terminates at around  $k_1 = 0.13$ , beyond which surface wrinkling gives way to a Biot instability, as shown in Fig. 8(a). In summary, a supercritical bifurcation arises when  $\bar{r} < \bar{r}_{tr}$ , beyond which it transitions to a subcritical bifurcation. Moreover, the intricate structure of these curves underscores the significant effect of fiber reinforcement.

As before, we can identify a domain where our post-buckling solution is applicable when the substrate is fiber-reinforced. We prescribe  $r = 0.05$  and consider two cases, i.e., either  $k_1 = 0.05$  or  $k_1 = 0.1$ . In both cases, the bifurcations are supercritical. We find  $\lambda_{cr} = 0.8788$ ,  $(nh)_{cr} = 0.6996$  and  $c_1 = 0.8945$  for  $r = 0.05$  and  $k_1 = 0.01$ . Further, the function  $\mathcal{I}(x_1, x_2)$  reaches a minimum at  $(\pi, 0)$  within the period  $[0, 2\pi] \times (-\infty, 0]$ . This gives  $\lambda_{cr} - \lambda = 0.0472$ , indicating the point where the fibers first experience compression. For  $r = 0.05$  and  $k_1 = 0.1$ , we obtain  $\lambda_{cr} = 0.8208$ ,  $(nh)_{cr} = 0.7625$  and  $c_1 = 0.6477$ . Meanwhile, the condition where the fibers are under compression reads  $\lambda_{cr} - \lambda = 0.1333$ . Based on these results, we show the associated bifurcation diagrams in Fig. 15. The blue curve for  $k_1 = 0.05$  stops at  $\lambda = 0.8316$  where the amplitude  $|A| \approx 0.23$ . However, the red curve remains valid in the sense that no fiber is under compression in our analysis until  $|A| \approx 0.454$ , which is far from the threshold. Therefore, the solution based on the weakly nonlinear analysis may lose validity before reaching the end point. For this reason, we only show the red curve up to  $\lambda = 0.79$ . It can be observed that when the substrate is fiber-reinforced, stiffer fibers experience compression much later.

### 5. Discussions

In the preceding sections, we derived analytically both the bifurcation condition and the amplitude equation governing post-buckling behavior, based on the nonlinear incremental theory of finite elasticity (Ogden, 1984; Goriely, 2017). Notably, the amplitude Eqs. (4.27) and (4.30) are obtained without introducing any *ad hoc* assumptions or fitting parameters. In this section, we compare our results with the literature and discuss potential extensions of our work.

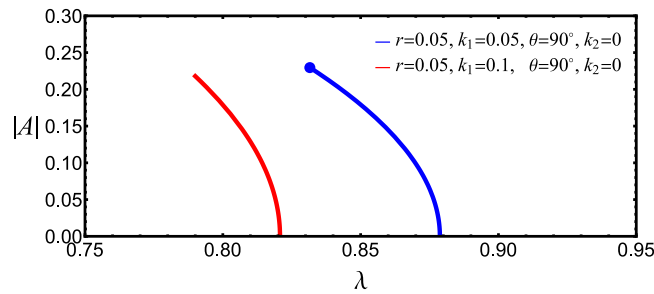


Fig. 15. Bifurcation diagrams based on the post-buckling solution derived in this section when the substrate is fiber-reinforced. Pitchfork supercritical bifurcations are found for both scenarios.

### 5.1. Comparisons with existing results

We apply the virtual work method to derive the amplitude equation at third-order nonlinearity (Fu and Devenish, 1996). The same result can alternatively be obtained using the Lyapunov–Schmidt–Koiter (LSK) method, originally introduced by Koiter (1945) and subsequently developed by Thompson (1963) and Thompson and Hunt (1973). A detailed exposition of the LSK method is also provided in Potier-Ferry (1987) and Triantafyllidis and Peek (1992). Post-buckling solutions obtained from both approaches exhibit good agreement with finite element simulations across various case studies (Jin et al., 2019; Chen and Jin, 2020). In particular, for a neo-Hookean film bonded to a neo-Hookean substrate under uniaxial compression, Cai and Fu (1999) and Hutchinson (2013) employed the virtual work and LSK methods, respectively, to derive the amplitude equation, both identifying a transition from supercritical to subcritical bifurcations at approximately  $r \approx 0.571$ . In the two scenarios considered in our study, the coefficient  $c_1$  depends on the parameters  $k_1$  and  $\theta$  that characterize the fiber properties. Setting  $k_1 = 0$  reduces the HGO model to the neo-Hookean model, thereby recovering the transition value associated with an isotropic neo-Hookean bilayer, as illustrated in Figs. 9(a) and 13(a). This agreement provides a first validation of our analytical post-buckling solutions.

Several previous studies on surface wrinkling of fiber-reinforced bilayers based on the theory of finite elasticity are particularly relevant to the present work (Nguyen et al., 2020; Altun et al., 2023; Mirandola et al., 2023). In Altun et al. (2023), the film is reinforced with fibers, whereas in Nguyen et al. (2020) and Mirandola et al. (2023), reinforcement is applied to the substrate. Although the compression considered in Altun et al. (2023) is growth-induced and the reinforcement involves a single family of fibers aligned in the in-plane direction, qualitative comparisons can still be drawn with our first case. Specifically, Altun et al. (2023) studied fibers oriented at  $\theta = 90^\circ$ , aligned along the  $X_3$ -direction rather than the  $X_2$ -direction as shown in Fig. 1. Our buckling analysis in Section 3.1 demonstrates that, for a fixed fiber orientation  $\theta = 90^\circ$ , increasing fiber stiffness destabilizes the structure, reducing the number of wrinkles and thereby increasing the wrinkle wavelength, consistent with the trends observed in Figure 7 of Altun et al. (2023). Furthermore, Altun et al. (2023) developed a numerical scheme to trace the post-buckling evolution and pattern transitions; however, determining the nature of the bifurcation remains challenging without analytical guidance. In practice, random geometric perturbations are often introduced to initiate bifurcation at the critical load. We emphasize that the analytical post-buckling solution (4.36) not only clarifies the role of fiber stiffness in the transition between subcritical and supercritical bifurcations but also provides an effective initial guess for numerical simulations. As reported by Dai et al. (2013), finite element schemes can converge within five iterations when initialized with an analytical solution.

When the substrate is anisotropic, a detailed linear analysis can be found in Nguyen et al. (2020) and Mirandola et al. (2023), that focuses on the case where the thin film is much stiffer than the substrate. In particular, Mirandola et al. (2023) derived leading-order expressions for the critical stretch and critical wavelength in the limit of a very stiff film. Accordingly, we present only one representative case study in Section 3.2, and all resulting bifurcation curves show qualitative agreement with the findings in Nguyen et al. (2020) and Mirandola et al. (2023). Nevertheless, we extend the discussion by revealing additional bifurcation phenomena in Fig. 8 for the case where the film is only moderately stiffer. These results provide insights into how various parameters influence mode transitions and can serve as a design guideline for tailoring buckling patterns in specific structures.

The main feature of the post-buckling evolution is that, close to bifurcation, the amplitude grows proportionally to the square root of the incremental strain, as shown in Eq. (4.36). Such a square root scaling can also be derived via geometric analysis by treating the thin stiff film as a layer that cannot change its length (or area in a three-dimensional setting) but can support bending (Pocivavsek et al., 2008). By directly fitting to finite element simulations, Nguyen et al. (2020) investigated the applicability of this square-root dependence to describe the evolution of surface wrinkling in the compliant HGO substrate coated with a stiff neo-Hookean film under compression. To facilitate a quantitative comparison with the post-buckling behavior shown in Figure 13 of Nguyen et al. (2020), we define the axial strain as  $\epsilon = 1 - \lambda$  and denote the deflection amplitude at the top surface ( $x_2 = h$ ) by  $\mathfrak{S}$ . The critical strain for surface wrinkling is denoted by  $\epsilon_{cr}$ , and the corresponding wavelength is given by  $\Lambda = 2\pi/n$  (note that we have fixed  $n = 1$  in our analysis). Nguyen et al. (2020) assumed a square root dependence of  $\mathfrak{S}/\Lambda = c_0 \sqrt{(\epsilon - \epsilon_{cr})/\epsilon_{cr}}$  with  $c_0$  a fitting parameter. They presented both finite element simulation results and the corresponding square root fitting curves for the evolution of  $\mathfrak{S}/\Lambda$  in their Fig. 13, considering the case  $\mu_{nH} \approx 100\mu_{HGO}$  ( $r \approx 0.01$ ),  $k_1 = 2\mu_{HGO}$  (i.e.,  $k_1 = 0.02$  in nondimensional form),  $k_2 = 0.8393$ , and three fiber orientations:  $\theta = 90^\circ, 60^\circ$ , and  $45^\circ$ .

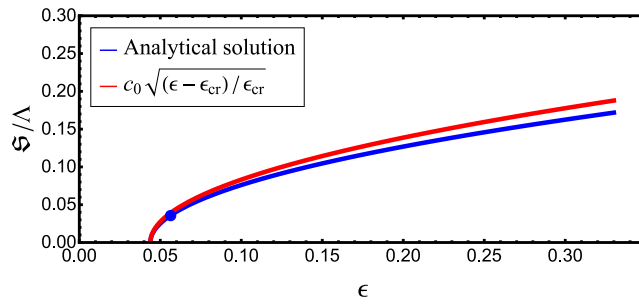


Fig. 16. The scaled amplitude  $\mathfrak{S}/\Lambda$  as a function of the applied compressive strain  $\epsilon$  when  $r_1 = 0.01$ ,  $k_1 = 0.02$ ,  $k_2 = 0$ , and  $\theta = 90^\circ$ . The blue curve represents the analytical solution given by (5.1) while the red curve corresponds to the fitting result reported by Nguyen et al. (2020).

As discussed in previous Sections 3 and 4, the effect of  $k_2$  is marginal. We therefore set  $k_2 = 0$  and consider the parameters  $r = 0.01$ ,  $k_1 = 0.02$ , and  $\theta = 90^\circ$ . From the bifurcation condition (3.19) we find that  $\epsilon_{cr} = 1 - \lambda_{cr} = 0.045885$  and  $(nh)_{cr} = 0.42246$ . Correspondingly, the analytical post-buckling solution (4.30) or (4.36) yields (to avoid confusion we mention that we have used the script style  $\epsilon$  to denote the small parameter in our post-buckling analysis, cf. (4.1))

$$\mathfrak{S}/\Lambda = \begin{cases} 0, & \text{if } \epsilon < \epsilon_{cr}, \\ 0.321188\sqrt{\epsilon - \epsilon_{cr}}, & \text{if } \epsilon \geq \epsilon_{cr}. \end{cases} \quad (5.1)$$

Additionally, we determine from Fig. 13 with  $\theta = 90^\circ$  in Nguyen et al. (2020) that the fitting parameter is determined to be  $c_0 \approx 13.5955$  such that  $\mathfrak{S}/\Lambda \approx 13.5955\sqrt{(\epsilon - \epsilon_{cr})/\epsilon_{cr}}$ .

Fig. 16 presents a comparison between the analytical solution (5.1) and the square root fitting expression. As shown in Figure 13 of Nguyen et al. (2020), the fitting model accurately captures the post-buckling evolution up to the point where surface wrinkles transition to a period-doubling instability. Consequently, the good agreement observed in Fig. 16 provides further validation of our analytical post-buckling solution. Although wrinkle formation begins to induce compressive stress in the fibers when the axial strain  $\epsilon$  exceeds approximately 0.0562 (indicated by the blue point in Fig. 16), the analytical solution remains accurate up to  $\epsilon \approx 0.12$ . Beyond this strain, surface wrinkling ceases to be energetically favorable, and period-doubling appears. For fiber orientations  $\theta = 60^\circ$  and  $45^\circ$ , a similarly good agreement between the analytical solution and the fitting model is observed; these results are omitted here for brevity.

The analytical post-buckling solution not only captures the nature of the bifurcation but, when compared with finite element simulations, provides a convenient framework for understanding the influence of various geometrical and material parameters on post-buckling evolution. Moreover, it identifies the point at which the bifurcation becomes subcritical as system parameters vary. Nguyen et al. (2020) also performed experiments on arterial wrinkling using pig carotid arteries to study the validity of the square root scaling for wrinkling and the linear scaling for folding, as proposed by Pociavsek et al. (2008). However, the fitting approach adopted in those studies does not reveal how material parameters collectively influence pattern evolution. Based on the fitting expression for post-buckling deflection shown in Figure 2 of Nguyen et al. (2020), we use our analytical solution (4.30) to estimate the modulus ratio  $r$  between the substrate and the film. Neglecting fiber reinforcement effects ( $k_1 = 0$ ), we find a good agreement with the observed wrinkling evolution when  $1/3 < r < 1/2$ , which is consistent with the known mechanical properties of the arterial media and adventitia layers (with the thin and soft intima layer excluded from the film–substrate approximation) (Giudici et al., 2021).

Additionally, the fitting expressions are limited in their ability to provide qualitative or quantitative predictions regarding the evolution of surface wrinkling under varying geometrical or material conditions. In this work, we derive new analytical post-buckling solutions that allow for the estimation of material properties of biological tissues from measurable wrinkling patterns. Furthermore, these solutions offer a robust benchmark for validating newly developed reduced theories or numerical models for fiber-reinforced soft materials.

### 5.2. When the fibers are non-symmetric

In line with previous work by Nguyen et al. (2020) and Mirandola et al. (2023), our initial model assumes a symmetric distribution of fiber families. To gain deeper insights into the role of asymmetry, we now broaden the framework to allow the two fiber families to adopt distinct preferred directions:

$$\mathbf{M} = \cos \theta_1 \mathbf{e}_1 + \sin \theta_1 \mathbf{e}_2, \quad \mathbf{M}' = \cos \theta_2 \mathbf{e}_1 - \sin \theta_2 \mathbf{e}_2, \quad (5.2)$$

where  $\theta_1$  and  $\theta_2$  are the angles between the fiber orientation and the  $X_1$ -axis. Using the reduced strain energy function (4.31), the Lagrange multiplier  $\bar{p}_{HGO}$  is given by

$$\bar{p}_{HGO} = \frac{\mu_{HGO}}{\lambda^2} + \frac{2k_1 \sin^2 \theta_1}{\lambda^2} \left( \lambda^2 \cos^2 \theta_1 - 1 + \frac{\sin^2 \theta_1}{\lambda^2} \right) + \frac{2k_1 \sin^2 \theta_2}{\lambda^2} \left( \lambda^2 \cos^2 \theta_2 - 1 + \frac{\sin^2 \theta_2}{\lambda^2} \right). \quad (5.3)$$

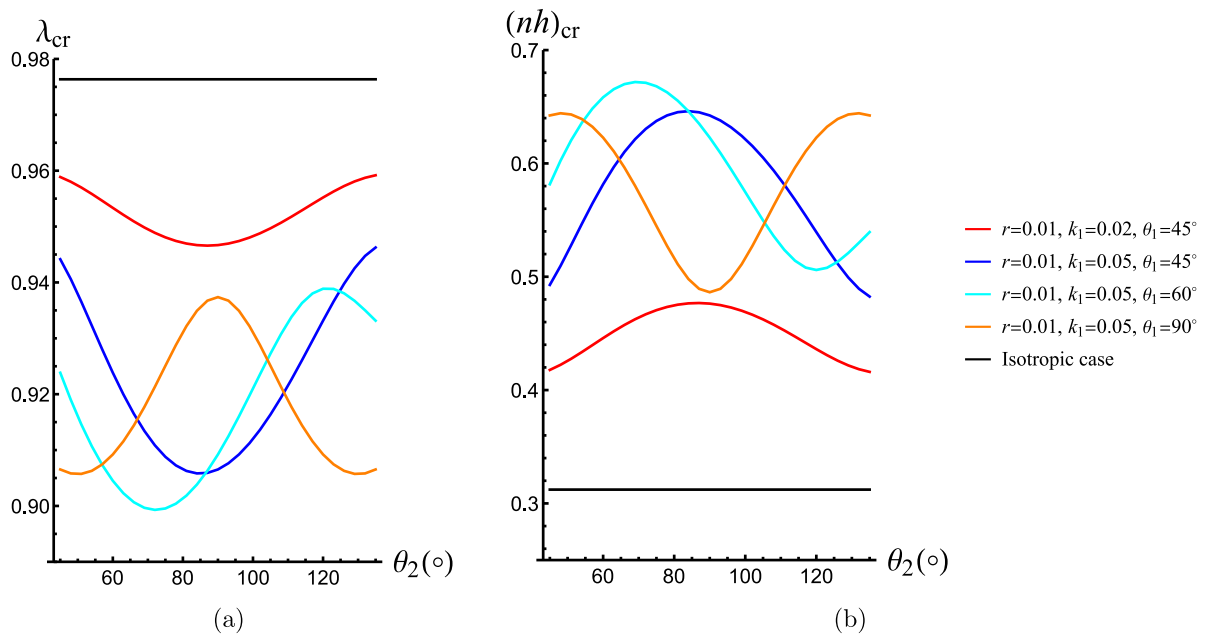


Fig. 17. The critical stretch  $\lambda_{cr}$  and the critical wavenumber  $(nh)_{cr}$  as functions of fiber angle  $\theta_2$  as  $r = 0.01$  with different values of  $k_1$  and  $\theta_1$ . The substrate is composed of an HGO material while the film is isotropic.

It is natural to extend the general derivations presented in Sections 2–4 to obtain both the bifurcation condition and the amplitude equation governing surface wrinkling. In this section, we briefly consider the second case where the substrate is fiber-reinforced, focusing on the influence of non-symmetric fiber distributions on the onset of surface wrinkling.

We find that the characteristic equation (3.5) is replaced by

$$\beta_4 s^4 + \beta_3 s^3 + \beta_2 s^2 + \beta_1 s + \beta_0 = 0, \tag{5.4}$$

where  $\beta_i$  ( $i = 0, 1, \dots, 4$ ) are constants related to the elastic moduli  $\mathcal{A}_{jilk}$  whose expressions are omitted. When  $\theta_1 = \theta_2$ , the coefficients  $\beta_1$  and  $\beta_3$  vanish, recovering the symmetric fiber case. In general, Eq. (5.4) admits four complex roots, two of which have positive real parts, while the other two have negative real parts. Apart from this distinction, the bifurcation condition can still be derived following the same procedure outlined in Section 3.

To understand the effect of non-symmetric fibers, we fix  $r = 0.01$  and plot in Fig. 17 the critical stretch  $\lambda_{cr}$  and the critical wavenumber  $(nh)_{cr}$  as functions of  $\theta_2$ , for varying  $\theta_1$  and  $k_1$ . The angle  $\theta_2$  is varied from  $45^\circ$  to  $135^\circ$  to avoid fiber compression. Notably, the case of a single family of fibers is recovered when  $\theta_1 + \theta_2 = \pi$ . For comparison, the results for the isotropic case are indicated by the black lines. We observe that the presence of non-symmetric fibers consistently delays the onset of surface wrinkling and increases the number of wrinkles, in agreement with the trends observed in Fig. 6. In particular, when  $k_1 = 0.05$ , the curves for  $\theta_1 = 45^\circ$  (blue),  $60^\circ$  (cyan), and  $90^\circ$  (orange) exhibit similar shapes, differing primarily in phase.

For symmetric fibers with  $\theta_1 = \theta_2 = \theta$ , it follows from equations (19) and (23) in Mirandola et al. (2023) that both the critical stretch and the critical wavenumber depend on  $\theta$  through a term  $\sin^2(4\theta)$ , which has a minimal period of  $\pi/4$ . This implies that  $\lambda_{cr}$  and  $(nh)_{cr}$  exhibit a quasi-periodic behavior with the same period  $\pi/4$ , although the peaks and valleys are not symmetric. Furthermore, this explains the non-monotonic behavior observed in all the curves in Fig. 6. Nevertheless, the apparent quasi-period seems to change from  $\pi/4$  to  $\pi/2$  in Fig. 17, suggesting a possible dependence on  $\theta_2$  (or  $\theta_1$ ) via a term like  $\cos 4\theta_2$ . Similarly, in the Case I discussed in Section 3.1, the critical stretch and wavenumber shown in Fig. 4 also display a quasi-period of  $\pi/2$ . To better understand these patterns, a more comprehensive asymptotic analysis is required to obtain mathematically consistent approximations for the critical state, which we leave for a separate study.

By considering a simple non-symmetric case, we have demonstrated that asymmetry can introduce intrinsic differences in the critical buckling condition. It is therefore expected that such asymmetry may also have a significant influence on the post-buckling behavior. This aspect will be explored in future studies.

### 5.3. When the fibers can support compression

We adopt the HGO model to describe fiber reinforcement (Holzapfel et al., 2000; Holzapfel and Ogden, 2010; Holzapfel et al., 2019). A key feature of this model is that fibers are unable to support compressive loads; when subjected to compression, the fibers become inactive, and the material response reduces to that of a neo-Hookean solid. To account for this feature, a tension–compression

switch is implemented to eliminate the fiber contribution under compressive strains (Holzapfel and Ogden, 2015). This assumption is appropriate for many biological tissues, such as skin and arteries (Holzapfel and Ogden, 2006). In view of this, we restrict our attention to fiber angles  $\theta > 45^\circ$ , ensuring that the fibers are under tension in the homogeneous state. This scenario is relevant to many real-world biological systems. For instance, wrinkling and folding in brain tissues often influence axonal growth, resulting in a fiber-reinforced white matter (substrate) with fiber orientations typically around  $\theta \approx 90^\circ$  (Solhtalab et al., 2025). We emphasize that the buckling and post-buckling results derived from the HGO model are not directly applicable when fibers are under compression. Accordingly, we make no claims regarding the buckling behavior of bent or wrinkled fibers in this study.

In practice, fiber distributions in both biological tissues and fiber-reinforced composites can be highly complex, making the presence of compressive fibers inevitable. Moreover, when the fiber stiffness greatly exceeds that of the surrounding matrix, the fiber's bending stiffness becomes significant and must be incorporated into the overall mechanical response (Kakaletsis et al., 2023). Additionally, fiber microbuckling plays a crucial role in shaping the macroscale buckling behavior (Li et al., 2018; Poullos and Niordson, 2016). Therefore, it is of great importance to develop theoretical models that account for the flexural and torsional elasticity of fibers in order to better understand how fiber configuration influences pattern formation and evolution of soft anisotropic materials.

Although beyond the scope of this study, we note that an effective approach to capturing the bending and twisting stiffnesses of embedded fibers is through the use of Cosserat elasticity for fiber-reinforced materials (Shirani and Steigmann, 2020; Steigmann et al., 2023). Recently, McAvoy and Steigmann (2025) developed an incremental theory for fibrous materials with a single family of fibers that resist extension, bending, and twisting. Their work provides a general framework for the buckling analysis of fiber-reinforced structures. As a case study, they examined compression-induced surface instability in a fibrous half-space. Unlike classical Biot instability, the presence of fibers introduces a dependence of the critical stretch on the wavenumber. Furthermore, McAvoy (2025) implemented Cosserat elasticity for fibrous materials within a three-dimensional finite element framework and explored novel buckling patterns induced by fiber reinforcement.

To compare, we emphasize that the case in which fibers can support compression is considerably more complex. The application of Cosserat elasticity necessitates additional kinematic descriptors to represent adequately fiber behavior. Nevertheless, this direction merits further investigation, as it offers the potential to yield deeper insights into the buckling and post-buckling behavior of fiber-reinforced soft tissues.

## 6. Conclusion

We studied surface instabilities of a fiber-reinforced bilayer under uniaxial compression. With advances in 3D printing technology, it has become convenient to fabricate anisotropic materials with tailored fiber orientations (Montanari et al., 2024). Two cases were considered, i.e., either the film or the substrate is composed of a fiber-reinforced material. Within the framework of finite elasticity, the nonlinear incremental equations were formulated, from which both the linear bifurcation analysis and the weakly nonlinear analysis can be carried out. An exact bifurcation condition was obtained that explains how fiber orientation and fiber stiffness regulate surface wrinkles at onset. In addition, we obtained an amplitude equation by a weakly nonlinear analysis. This amplitude equation describes how the wrinkled morphology grows beyond the bifurcation point and further can provide a criterion for the type of bifurcation observed.

To capture fiber-reinforcement, we employed the Holzapfel–Gasser–Ogden model which was first proposed for arteries (Holzapfel et al., 2000; Holzapfel and Ogden, 2010). Note that in this model the fibers cannot support compression. Therefore, we identified allowable values of the stretch  $\lambda$  and the fiber angle  $\theta$  where fibers play a role. Otherwise, when the fiber angle is below the transition angle, the anisotropic bilayer considered here will reduce to the well-known case of a neo-Hookean bilayer.

When the film is fiber-reinforced, wrinkling instability can be either promoted or suppressed by adjusting the fiber stiffness and orientation. In particular, increasing fiber stiffness consistently reduces the number of wrinkles. To illustrate the effect of fiber orientation, we presented two phase diagrams in Fig. 5. Once the applied compressive strain exceeds the critical threshold, the system enters a post-buckling state. Using the amplitude Eq. (4.27), we analyzed how fiber properties influence the transition modulus ratio and identified the shift between subcritical and supercritical bifurcations for various fiber angles. Additionally, we determined the admissible domain of the post-buckling solution using the HGO model and presented the corresponding bifurcation diagrams.

When the substrate is fiber-reinforced, fibers can simultaneously retard or promote surface wrinkling, depending on their properties. This phenomenon parallels the process of skin wrinkling with aging, where the dermis loses stiffness due to collagen fiber degradation (Kruglikov and Scherer, 2018). A key finding was the existence of a transition fiber angle at which surface wrinkling gives way to Biot instability, characterized by a critical mode tending to infinity. To illustrate this behavior, we presented two phase diagrams in Fig. 8, mapping the regions of different instability modes in the  $(\theta, k_1)$ - and  $(\theta, r)$ - planes. Additionally, we identified the transition between subcritical and supercritical bifurcations and provided a bifurcation diagram derived from our post-buckling analysis. Our results show that subcritical bifurcation is more likely to emerge when fiber stiffness dominates the substrate, offering insight into the emergence of creasing and folding patterns in biological tissues such as the brain (Stewart et al., 2016; Solhtalab et al., 2025).

In both cases, we have validated our buckling and post-buckling results both qualitatively and quantitatively against existing results reported in Cai and Fu (1999), Nguyen et al. (2020), Altun et al. (2023) and Mirandola et al. (2023). Specifically, the analytical post-buckling solutions derived in this study involve no *ad hoc* assumptions or fitting parameters. Furthermore, the analytical solution provides a convenient way for obtaining the post-buckling evolution and understanding the influence of anisotropy on the post-buckling deflection. Additionally, it serves as a benchmark for validating reduced models and finite element

schemes for fibrous materials, and provides a solid foundation for further analytical investigations into period-doubling secondary bifurcations (Fu and Cai, 2015).

For  $\theta > 45^\circ$ , fibers are expected to resist lateral deformation. Interestingly, when the film is fiber-reinforced, there exists a critical fiber angle at which the fibers become structurally undetectable, as illustrated in Fig. 4. This phenomenon is analogous to the “magic angle” observed in inflated fiber-reinforced cylindrical tubes, where deformation is entirely suppressed (Goriely and Tabor, 2013). Similarly, when the fiber orientation falls within a specific range, localized bulging in inflated tubes becomes impossible (Wang and Fu, 2018). However, in thick fiber-reinforced tissues, where the material behaves as a substrate rather than a thin film, this special angle disappears, highlighting the highly nonlinear influence of fibers on buckling and post-buckling behavior. In addition, when bifurcation is subcritical, Shen et al. (2024) numerically demonstrated that creases emerge as a consequence of an unstable deformation path. However, the long-term evolution of these patterns remains an open question, requiring further theoretical and experimental investigations.

### CRedit authorship contribution statement

**Yang Liu:** Writing – original draft, Methodology, Investigation, Funding acquisition, Formal analysis, Conceptualization. **Rui-Cheng Liu:** Writing – review & editing, Validation, Investigation. **Wanyu Ma:** Writing – review & editing, Investigation, Formal analysis. **Alain Goriely:** Writing – review & editing, Methodology, Investigation, Funding acquisition, Formal analysis, Conceptualization.

### Declaration of competing interest

The authors declare that they have no known competing financial interests or personal relationships that could have appeared to influence the work reported in this paper.

### Acknowledgments

This work was supported by grants from the National Natural Science Foundation of China (Project Nos. 12072227 and 12021002). Y.L. and A.G. acknowledge the UKRI Horizon Europe Guarantee MSCA (Marie Skłodowska-Curie Actions) Postdoctoral Fellowship (EPSRC Grant No. EP/Y030559/1). For the purpose of Open Access, the author has applied a CC BY public copyright license to any Author Accepted Manuscript (AAM) version arising from this submission.

### Data availability

Data will be made available on request.

### References

- Alawiye, H., Farrell, P.E., Goriely, A., 2020. Revisiting the wrinkling of elastic bilayers II: Post-bifurcation analysis. *J. Mech. Phys. Solids* 143, 104053.
- Alawiye, H., Kuhl, E., Goriely, A., 2019. Revisiting the wrinkling of elastic bilayers I: linear analysis. *Phil. Trans. R. Soc. A* 377, 20180076.
- Altun, C., Gürses, E., Dal, H., 2023. Growth-induced instabilities for transversely isotropic hyperelastic materials. *Mech. Soft Mater* 5 (1), 7.
- Barnes, M., Feng, F., Biggins, J., 2023. Surface instability in a nematic elastomer. *Phys. Rev. Lett.* 131, 238101.
- Ben Amar, M., Goriely, A., 2005. Growth and instability in elastic tissues. *J. Mech. Phys. Solids* 53, 2284–2319.
- Bigoni, D., Ortiz, M., Needleman, A., 1997. Effect of interfacial compliance on bifurcation of a layer bonded to a substrate. *Int. J. Solids Struct.* 34, 4305–4326.
- Biot, M.A., 1963. Surface instability of rubber in compression. *Appl. Sci. Res. Sect. A* 12, 168–182.
- Biot, M.A., 1965. *Mechanics of Incremental Deformations*. John Wiley & Sons Inc., New York.
- Budday, S., Steinmann, P., Kuhl, E., 2014. The role of mechanics during brain development. *J. Mech. Phys. Solids* 72, 75–92.
- Budday, S., Steinmann, P., Kuhl, E., 2015. Secondary instabilities modulate cortical complexity in the mammalian brain. *Phil. Mag.* 95 (28–30), 3244–3256.
- Cai, Z.X., Fu, Y.B., 1999. On the imperfection sensitivity of a coated elastic half-space. *Proc. R. Soc. Lond. A* 455 (1989), 3285–3309.
- Cai, Z.X., Fu, Y.B., 2000. Exact and asymptotic stability analyses of a coated elastic half-space. *Int. J. Solids Struct.* 37, 3101–3119.
- Cai, Z.X., Fu, Y.B., 2019. Effects of pre-stretch, compressibility and material constitution on the period-doubling secondary bifurcation of a film/substrate bilayer. *Int. J. Non-Linear Mech.* 115, 11–19.
- Chadwick, P., Ogden, R., 1971. On the definition of elastic moduli. *Arch. Ration. Mech. Anal.* 44, 41–53.
- Chavoshnejad, P., Foroughi, A.H., Dhandapani, N., German, G.K., Razavi, M.J., 2021. Effect of collagen degradation on the mechanical behavior and wrinkling of skin. *Phys. Rev. E* 104 (3), 034406.
- Cheewaruangroj, N., Biggins, J.S., 2019. Pattern selection when a layer buckles on a soft substrate. *Soft Matter* 15, 3751–3770.
- Chen, Z., Chen, W.Q., Song, J.Z., 2017. Buckling of a stiff thin film on an elastic graded compliant substrate. *Proc. R. Soc. A* 473, 20170410.
- Chen, X., Hutchinson, J.M., 2004. Herringbone buckling patterns of compressed thin films on compliant substrates. *J. Appl. Mech.* 71 (5), 597–603.
- Chen, Y., Jin, L., 2020. From continuous to snapping-back buckling: A post-buckling analysis for hyperelastic columns under axial compression. *Int. J. Non-Linear Mech.* 125, 103532.
- Cheng, H.Y., Zhang, Y.H., Huang, K.C., Rogers, J.A., Huang, Y.G., 2014. Buckling of a stiff thin film on a pre-strained bi-layer substrate. *Int. J. Solids Struct.* 51, 3113–3118.
- Ciarletta, P., 2014. Wrinkle-to-fold transition in soft layers under equi-biaxial strain: A weakly nonlinear analysis. *J. Mech. Phys. Solids* 73, 118–133.
- Ciarletta, P., Fu, Y.B., 2015. A semi-analytical approach to biot instability in a growing layer: strain gradient correction, weakly non-linear analysis and imperfection sensitivity. *Int. J. Non Linear Mech.* 75, 38–45.
- Cui, Y., 2016. Wrinkles in electronics. *IEEE Trans. Electron. Devices* 63 (9), 3372–3384.
- Dai, H.-H., Liu, Y., 2014. Critical thickness ratio for buckled and wrinkled fruits and vegetables. *Europhys. Lett.* 108 (4), 44003.

- Dai, H.H., Wang, Y.B., Wang, F.F., 2013. Primary and secondary bifurcations of a compressible hyperelastic layer: Asymptotic model equations and solutions. *Int. J. Non-Linear Mech.* 52, 58–72.
- Eskandari, M., Javili, A., Kuhl, E., 2016. Elastosis during airway wall remodeling explains multiple co-existing instability patterns. *J. Theoret. Biol.* 403, 209–218.
- Fu, Y.B., 1995. Resonant-triad instability of a pre-stressed incompressible elastic plate. *J. Elasticity* 41, 13–37.
- Fu, Y.B., Cai, Z.X., 2015. An asymptotic analysis of the period-doubling secondary bifurcation in a film/substrate bilayer. *SIAM J. Appl. Math.* 75 (6), 2381–2395.
- Fu, Y.B., Ciarletta, P., 2015. Buckling of a coated elastic half-space when the coating and substrate have similar material properties. *Proc. R. Soc. A* 471, 20140979.
- Fu, Y.B., Devenish, B., 1996. Effects of pre-stresses on the propagation of nonlinear surface waves in an incompressible elastic half-space. *Q. J. Mech. Appl. Math.* 49 (1), 65–80.
- Fu, Y.B., Ogden, R., 1999. Nonlinear stability analysis of pre-stressed elastic bodies. *Contin. Mech. Therm.* 11, 141–172.
- Gasser, T.C., Holzapfel, G.A., Ogden, R.W., 2006. Hyperelastic modelling of arterial layers with distributed collagen fibre orientations. *J. R. Soc. Interface* 3 (6), 15–35.
- Gent, A.N., 1996. A new constitutive relation for rubber. *Rubber Chem. Technol.* 69, 59–61.
- Genzer, J., Groenewold, J., 2006. Soft matter with hard skin: From skin wrinkles to templating and material characterization. *Soft Matter* 2 (4), 310–323.
- Giudici, A., Khir, A.W., Szafron, J.M., SpronckFrom, B., 2021. Uniaxial testing of isolated layers to a tri-layered arterial wall: a novel constitutive modelling framework. *Ann. Biomed. Eng.* 49 (9), 2454–2467.
- Goriely, A., 2017. *The Mathematics and Mechanics of Biological Growth*. Springer, New York.
- Goriely, A., Tabor, M., 2013. Rotation, inversion and perversion in anisotropic elastic cylindrical tubes and membranes. *Proc. R. Soc. A* 469, 20130011.
- Guo, Y., Nie, G., 2023. Surface wrinkling of a film on an anisotropic substrate. *Mech. Adv. Mater. Struct.* 1–9.
- Han, D., Li, W., Hou, Y., Chen, X., Shi, H., Meng, F., Zhang, L., Chen, X., 2024. Controllable wrinkling inspired multifunctional metamaterial for near-field and holographic displays. *Laser Photonics Rev.* 18, 2300879.
- Hill, M.R., Duan, X., Gibson, G.A., Watkins, S., Robertson, A.M., 2012. A theoretical and non-destructive experimental approach for direct inclusion of measured collagen orientation and recruitment into mechanical models of the artery wall. *J. Biomech.* 45 (5), 762–771.
- Holland, M.A., Budday, S., Li, G., Shen, D., Goriely, A., Kuhl, E., 2020. Folding drives cortical thickness variations. *Eur. Phys. J. Spec. Top.* 229, 2757–2778.
- Holzapfel, G.A., Gasser, T.C., Ogden, R.W., 2000. A new constitutive framework for arterial wall mechanics and a comparative study of material models. *J. Elasticity* 61, 1–48.
- Holzapfel, G.A., Ogden, R.W., 2006. *Mechanics of Biological Tissue*. Springer, Berlin/New York.
- Holzapfel, G.A., Ogden, R.W., 2010. Constitutive modelling of arteries. *Proc. R. Soc. A* 466 (2118), 1551–1597.
- Holzapfel, G.A., Ogden, R.W., 2015. On the tension–compression switch in soft fibrous solids. *Eur. J. Mech. A Solids* 49, 561–569.
- Holzapfel, G.A., Ogden, R.W., 2017. *Biomechanics: Trends in Modeling and Simulation*. Springer, Switzerland.
- Holzapfel, G.A., Ogden, R.W., Sherifova, S., 2019. On fibre dispersion modelling of soft biological tissues: a review. *Proc. R. Soc. A* 475 (2224), 20180736.
- Horgan, C.O., Saccomandi, G., 2005. A new constitutive theory for fiber-reinforced incompressible nonlinearly elastic solids. *J. Mech. Phys. Solids* 53, 1985–2015.
- Huang, R., 2005. Kinetic wrinkling of an elastic film on a viscoelastic substrate. *J. Mech. Phys. Solids* 53, 63–89.
- Hutchinson, J.W., 2013. The role of nonlinear substrate elasticity in the wrinkling of thin films. *Proc. R. Soc. A* 371 (1993), 20120422.
- Hutchinson, J.W., Koiter, W.T., 1970. Postbuckling theory. *Appl. Mech. Rev.* 23 (12), 1353–1366.
- Im, S.H., Huang, R., 2008. Wrinkle patterns of anisotropic crystal films on viscoelastic substrates. *J. Mech. Phys. Solids* 56 (12), 3315–3330.
- Jia, F., Pearce, S., Goriely, A., 2018. Curvature delays growth-induced wrinkling. *Phys. Rev. E* 98, 033003.
- Jin, L.S., Liu, Y., Cai, Z.X., 2019. Post-buckling analysis on growing tubular tissues: A semi-analytical approach and imperfection sensitivity. *Int. J. Solids Struct.* 162, 121–134.
- Kakaletsis, S., Lejeune, E., Rausch, M., 2023. The mechanics of embedded fiber networks. *J. Mech. Phys. Solids* 181, 105456.
- Kim, P., Abkarian, M., Stone, H.A., 2011. Hierarchical folding of elastic membranes under biaxial compressive stress. *Nat. Mater* 10 (12), 952–957.
- Koiter, W.T., 1945. On the Stability of Elastic Equilibrium (in Dutch with English Summary) (Thesis). Technische Hooze School, Delft, The Netherlands.
- Kruglikov, L.L., Scherer, P.E., 2018. Skin aging as a mechanical phenomenon: the main weak links. *Nutr. Heal. Aging* 4, 291–307.
- Lee, J., Jung, S., Kim, W., 2021. Dependence of the effective surface tension of liquid phase eutectic gallium indium on wrinkles of the surface oxide. *Extrem. Mech. Lett.* 48, 101386.
- Lee, G., Zarei, M., Wei, Q., Zhu, Y., Lee, S.G., 2022. Surface wrinkling for flexible and stretchable sensors. *Small* 18, 2203491.
- Li, B., Cao, Y.P., Feng, X.Q., Gao, H., 2011. Surface wrinkling of mucosa induced by volumetric growth: theory, simulation and experiment. *J. Mech. Phys. Solids* 59 (4), 758–774.
- Li, B., Cao, Y.P., Feng, X.Q., Gao, H., 2012. Mechanics of morphological instabilities and surface wrinkling in soft materials: a review. *Soft Matter* 8 (5728), 114–122.
- Li, J., Slesarenko, V., Galich, P.I., Rudykh, S., 2018. Instabilities and pattern formations in 3D-printed deformable fiber composites. *Compos. Part B: Eng.* 148, 114–122.
- Li, Z.W., Zhai, Y., Wang, Y., Wendland, G.M., Yin, X.B., Xiao, J.L., 2017. Harnessing surface wrinkling-cracking patterns for tunable optical transmittance. *Adv. Opt. Mater* 5 (19), 1700425.
- Liu, Y., Dai, H.-H., 2014. Compression of a hyperelastic layer-substrate structure: Transitions between buckling and surface modes. *Internat. J. Engrg. Sci.* 80, 74–89.
- Liu, Y., Goriely, A., Mihai, L.A., 2025. Elephant trunk wrinkles: A mathematical model of function and form. *Nonlinearity* 38 (3), 035004.
- Liu, Y., Ji, Q., Goriely, A., 2024a. Surface wrinkling of a hyperelastic half-space coated by a liquid crystal elastomer film. *Int. J. Solids Struct.* 299, 112895.
- Liu, R.C., Jin, L.S., Liu, Y., Cai, Z.X., 2022a. An experimental study of morphological formation in bilayered tubular structures driven by swelling/growth. *Math. Mech. Solids* 27 (8), 1569–1591.
- Liu, Y., Liang, T., Fu, Y., Xie, Y.-X., Wang, Y.-S., 2022b. A novel buckling pattern in periodically porous elastomers with applications to elastic wave regulations. *Extrem. Mech. Lett.* 54, 101781.
- Liu, X., Liu, Y., Feng, X.-Q., 2022c. Radial wrinkling of viscoelastic film–substrate systems. *Int. J. Solids Struct.* 249, 111689.
- Liu, R.C., Liu, Y., Goriely, A., 2024b. Surface wrinkling of a film coated to a graded substrate. *J. Mech. Phys. Solids* 186, 105603.
- Liu, Y., Zhang, Z., Devillanova, G., Cai, Z., 2020. Surface instabilities in graded tubular tissues induced by volumetric growth. *Int. J. Non-Linear Mech.* 127, 103612.
- Lynch, B., Pigeon, H., Le Blay, H., Brizion, S., Bastien, P., Bornschlöggl, T., Domanov, Y., 2022. A mechanistic view on the aging human skin through ex vivo layer-by-layer analysis of mechanics and microstructure of facial and mammary dermis. *Sci. Rep.* 12 (849).
- McAvoy, R.C., 2025. Exotic buckling patterns in fiber-reinforced materials: Numerical simulations of Cosserat elasticity. *Int. J. Solids Struct.* 312, 113272.
- McAvoy, R.C., Steigmann, D.J., 2025. Incremental deformations and bifurcation of elastic solids reinforced by fibers with intrinsic extensional, flexural, and torsional elasticity. *J. Appl. Mech.* 92 (1), 011006.
- Mirandola, A., Cutolo, A., Carotenuto, A.R., Nguyen, N., Pociavsek, L., Fraldi, M., Deseri, L., 2023. Toward new scaling laws for wrinkling in biologically relevant fiber-reinforced bilayers. *J. Appl. Phys.* 134 (15).
- Montanari, M., Hamaied, R., Gao, C., Bertolin, C., Spagnoli, A., 2024. An exploration into surface wrinkling in 3D printing inspired orthotropic bilayer systems. *Int. J. Solids Struct.* 298, 112862.

- Nguyen, N., Nath, N., Deseri, L., Tzeng, E., Velankar, S.S., Pociavsek, L., 2020. Wrinkling instabilities for biologically relevant fiber-reinforced composite materials with a case study of Neo-Hookean/Ogden–Gasser–Holzapfel bilayer. *Biomech. Model. Mech.* 19, 2375–2395.
- Ogden, R.W., 1984. *Non-Linear Elastic Deformations*. Ellis Horwood, New York.
- Pociavsek, L., Dellsy, R., Kern, A., Johnson, S., Lin, B., Lee, K.Y.C., Cerda, E., 2008. Stress and fold localization in thin elastic membranes. *Science* 320, 912–916.
- Pociavsek, L., Pugar, J., O’Dea, R., Ye, S.-H., Wagner, W., Tzeng, E., Velankar, S., Cerda, E., 2018. Topography-driven surface renewal. *Nat. Phys.* 14, 948–953.
- Polukhov, E., Pytel, L., Keip, M.-A., 2023. Swelling-induced pattern transformations of periodic hydrogels—from the wrinkling of internal surfaces to the buckling of thin films. *J. Mech. Phys. Solids* 175, 105250.
- Potier-Ferry, M., 1987. Foundations of elastic postbuckling theory. In: *Buckling and Post-Buckling*. In: *Lecture Notes in Physics*, vol. 1–82, Springer, Berlin, Heidelberg.
- Poulios, K., Niordson, C.F., 2016. Homogenization of long fiber reinforced composites including fiber bending effects. *J. Mech. Phys. Solids* 94, 433–452.
- Shen, J., Fu, Y.B., Pirrera, A., Groh, R.M.G., 2024. Wrinkling of differentially growing bilayers with similar film and substrate moduli. *J. Mech. Phys. Solids* 193, 105900.
- Shield, T.W., Kim, K.S., Shield, R.T., 1994. The buckling of an elastic layer bonded to an elastic substrate in plane strain. *J. Appl. Mech.* 61 (2), 231–235.
- Shirani, M., Steigmann, D.J., 2020. A cosserat model of elastic solids reinforced by a family of curved and twisted fibers. *Symmetry* 12 (7), 1133.
- Solhtalab, A., Foroughi, A.H., Pierotich, L., Razavi, M.J., 2025. Stress landscape of folding brain serves as a map for axonal pathfinding. *Nat. Commun.* 16 (1), 1187.
- Song, J., 2010. Herringbone buckling patterns of anisotropic thin films on elastomeric substrates. *Appl. Phys. Lett.* 96 (5).
- Steigmann, D.J., Birsan, M., Shirani, M., 2023. A cosserat model for fiber-reinforced elastic plates. In: *Sixty Shades of Generalized Continua: Dedicated To the 60th Birthday of Prof. Victor a. Eremeyev*. Springer, pp. 663–686.
- Stewart, P.S., Waters, S.L., Sayed, T.El., Vella, D., Goriely, A., 2016. Wrinkling, creasing, and folding in fiber-reinforced soft tissues. *Extrem. Mech. Lett.* 8, 22–29.
- Sun, Y., Choi, W.M., Jiang, H., Huang, Y.Y., Rogers, J.A., 2006. Controlled buckling of semiconductor nanoribbons for stretchable electronics. *Nat. Nanotechnol.* 1 (3), 201–207.
- Taffetani, M., Hennessy, M.G., 2024. Curvature controls beading in soft coated elastic cylinders: Finite wavemode instability and localized modulations. *J. Mech. Phys. Solids* 187, 105606.
- Tan, Y., Hu, B., Song, J., Chu, Z., Wu, W., 2020. Bioinspired multiscale wrinkling patterns on curved substrates: An overview. *Nano- Micro Lett.* 12 (101).
- Thompson, J.M.T., 1963. Basic principles in the general theory of elastic stability. *J. Mech. Phys. Solids* 11, 13–25.
- Thompson, J.M.T., Hunt, G.W., 1973. *A General Theory of Elastic Stability*. John Wiley & Sons, London, UK.
- Triantafyllidis, N., Peek, R., 1992. On stabling and the worst imperfection shape in solid with nearly simultaneous eigenmodes. *Int. J. Solids Struct.* 29, 2281–2299.
- Wang, S., Demirci, N., Holland, M.A., 2021. Numerical investigation of biomechanically coupled growth in cortical folding. *Biomech. Model. Mech.* 20 (2), 555–567.
- Wang, J., Fu, Y.B., 2018. Effect of double-fibre reinforcement on localized bulging of an inflated cylindrical tube of arbitrary thickness. *J. Engrg. Math.* 109, 21–30.
- Yang, S., Khare, K., Lin, P.C., 2010. Harnessing surface wrinkle patterns in soft matter. *Adv. Funct. Mater.* 20, 2550–2564.
- Yin, J., Chen, X., Sheinman, I., 2009. Anisotropic buckling patterns in spheroidal film/substrate systems and their implications in some natural and biological systems. *J. Mech. Phys. Solids* 57 (9), 1470–1484.
- Yin, S.F., Li, B., Cao, Y.P., Feng, X.Q., 2018. Surface wrinkling of anisotropic films bonded on a compliant substrate. *Int. J. Solids Struct.* 141, 219–231.
- Zhang, T., 2017. Symplectic analysis for wrinkles: a case study of layered neo-hookean structures. *J. Appl. Mech.* 84 (7), 071002.
- Zhang, Z., Zhang, T., Zhang, Y.W., Kim, K., Gao, H., 2012. Strain-controlled switching of hierarchically wrinkled surfaces between superhydrophobicity and superhydrophilicity. *J. Am. Chem. Soc.* 134 (5), 2753–2760.
- Zhao, Y.C., Fang, F., 2024. Bio-inspired hierarchical wrinkles for tunable infrared reflectance. *Surf. Interfaces* 45, 103832.
- Zhao, Y., Feng, B., Lee, J., Lu, N., Pierce, D.M., 2020. A multi-layered model of human skin elucidates mechanisms of wrinkling in the forehead. *J. Mech. Behav. Biomed. Mater.* 105, 103694.
- Zhao, Y., Han, X., Li, G., Lu, C., Cao, Y., Feng, X.Q., Gao, H., 2015. Effect of lateral dimension on the surface wrinkling of a thin film on compliant substrate induced by differential growth/swelling. *J. Mech. Phys. Solids* 83, 129–145.
- Zhou, M., Cai, Z., Fu, Y., 2022. Post-buckling of an elastic half-space coated by double layers. *Math. Mech. Solids* 27 (2), 193–209.